Title
Field-Programmable Acoustic Platform for Deep, Subwavelength-Resolution Patterning of Micro-Objects into Complex and Non-Periodic Shapes

Author
Tung, Kuan-Wen

Publication Date
2020

UNIVERSITY OF CALIFORNIA

Los Angeles

Field-Programmable Acoustic Platform for Deep, Subwavelength-Resolution Patterning of Micro-Objects into Complex and Non-Periodic Shapes

A dissertation submitted in partial satisfaction of the

requirements for the degree Doctor of Philosophy

in Mechanical Engineering

by

Kuan-Wen Tung

2020

ABSTRACT OF THE DISSERTATION

Field-Programmable Acoustic Platform for Deep, Subwavelength-Resolution Patterning of Micro-Objects into Complex and Non-Periodic Shapes

by

Kuan-Wen Tung

Doctor of Philosophy in Mechanical Engineering

University of California, Los Angeles, 2020

Professor Pei-Yu Chiou, Chair

Manipulation of biological micro-objects *in vitro* is essential for many biomedical applications, such as the study of cells' or molecular interaction, single-cell analysis, drug delivery, and tissue engineering. There are various physical mechanisms employed to achieve the manipulation; electrokinetic, optical, magnetic, hydrodynamic, and acoustic mechanisms are all conventional examples that have been deeply researched. In comparison, acoustics has been demonstrated to have superior biocompatibility and wide range of operable sizes of target, making it an attractive option to be widely utilized in many applications. On the other hand, acoustics suffers from limited Degree-of-Freedom (DOF) in objects' manipulation due to the fundamental constraint stemmed from the principle that conventional acoustic devices built upon. Furthermore, acoustic patterning

of micro-objects that allows not only real-time, versatile adjustment but also re-configuration to the patterning profile has not yet been realized. This re-configurable feature is particularly crucial in taking the acoustic manipulation technology from the current research phase to the next stage for broader applications.

For this dissertation, two important concepts are investigated and realized to overcome the acoustic limitations described. The first concept explores a new field of acoustofluidics where a novel manipulation platform is developed, making a breakthrough to the conventional approach in objects' manipulation in achieving highly complex and non-periodic patterning shapes. The second concept involves integration of a photothermal mechanism with the developed acoustic platform which allows the acoustic potential field to be adjusted and re-configured, leading to a programmable platform for highly complex patterning of micro-objects.

In the first concept, a new acoustofluidic field using deep, sub-wavelength approach is exploited. Different from the traditional techniques that rely on using standing waves to generate the acoustic potential wells only spaced periodically at half the wavelength, the new approach can generate the acoustic wells spaced arbitrarily within half the wavelength. To achieve such approach, we developed a "Complaint Membrane Acoustic Patterning" (CMAP) platform utilizing an air-embedded, viscoelastic Polydimethylsiloxane (PDMS) structure to precisely control the wave fronts by providing barriers to incoming waves using acoustic impedance mismatch between air and PDMS, creating a non-uniform energy field and thus the acoustic wells. The embedded air cavities dictate the shape of the wells. Since the cavities can be fabricated into any geometry, complicated profiles of the wells can be realized. As experiments have

demonstrated, we succeeded in the patterning of micro-polystyrene beads and HeLa cells into various numeric-letter shapes with resolution one tenth of the wavelength across a large 3 x 3 mm^2 area.

In the second concept, a photothermal mechanism is integrated into the CMAP platform to achieve re-configurable patterning of micro-objects. A layer of light absorbing hydrogenated amorphous silicon (a-Si:H) is incorporated into the bottom of CMAP's PDMS structure, where the cavities are initially fluid-filled. By focusing a laser light onto the a-Si:H layer to evaporate the fluid within the cavities selectively, we can modify where in the PDMS structure would contain fluid or air. Cavities containing air can also be reverted to contain fluid. Since the acoustic impedance of PDMS matches closely to that of water, acoustic waves could pass through easily. This way, we have the versatility in shaping and re-shaping an array of air cavities, permitting the generation of adjustable potential profile of the acoustic wells which leads to field-programmable functionality for highly complex and non-periodic patterning.

The dissertation of Kuan-Wen Tung is approved.

Benjamin M. Wu

Dino Di Carlo

Jeffrey D. Eldredge

Pei-Yu Chiou, Committee Chair

University of California, Los Angeles

2020

Contents

LIST OF FIGURES

Chapter 1

Chapter 2

Chapter 3

ACKNOWLEDGEMENTS

I would like to express my sincere gratitude to all who have provided me invaluable learning experience and supports during the course of my Ph.D. study at the University of California, Los Angeles.

First, I would like to thank my adviser, Prof. Pei-Yu Chiou, who provided me dedicated academic guidance to my researches and the opportunity as the first student in our lab to work on acoustofluidics, a privilege in leading the foundation knowledge that paves the way for all prospective acoustofluidic projects. While the journey has been challenging, his training to problem-solving approach has been substantial and rewarding. Learning to tackle a problem from its fundamental root cause has taught me where the most powerful solution stems from.

Second, I would like to thank my committee members who have provided me invaluable knowledge and recommendations. I thank Prof. Benjamin M. Wu for his expertise in cell biology that greatly facilitated my research in cell patterning. I also thank Prof. Dino Di Carlo and Prof. Jeffrey D. Eldredge for their expertise in microelectromechanical systems (MEMS) and microfluids which contributed greatly to my device design.

Third, I would like to thank my colleagues for their supports in advancing my researches. I thank Pei-Shan Chung and Sidhant Tiwari for their contributions to my acoustic research simulations. I thank Cong Wu and Tianxing Man for their contributions to my cell experiment, including cell preparation, culturing, and viability assessments. I also thank Tan Xing Haw for his supports on my acoustic device fabrication approach.

Finally, I would like to thank Prof. Yuan-Fang Chou and Prof. Fu-ling Yang of National Taiwan University for their knowledge in polymer engineering and fluid mechanics that provided substantial supports to the analysis of my device operation.

VITA

Education

2007-2011 B.S., Mechanical Engineering

Lehigh University

Bethlehem, PA USA

2011-2012 M.S., Mechanical Engineering

University of Illinois at Urbana-Champaign

Champaign, IL USA

Publication

- **Tung, K.W.** and Chiou, P.Y., 2020. Field-Programmable Acoustic Array for Patterning Micro-objects. Applied Physics Letters, (*under minor revision*).

- **Tung, K.W**., Chung, P.S., Wu, C., Man, T., Tiwari, S., Wu, B., Chou, Y.F., Yang, F.L. and Chiou, P.Y., 2019. Deep, sub-wavelength acoustic patterning of complex and non-periodic shapes on soft membranes supported by air cavities. Lab on a Chip, 19(21), pp.3714-3725.

- Zhu, X., **Tung, K.W.** and Chiou, P.Y., 2017. Heavily doped silicon electrode for dielectrophoresis in high conductivity media. Applied Physics Letters, 111(14), p.143506

- Lin, M.Y., Wu, Y.C., Lee, J.A., **Tung, K.W**., Zhou, J., Teitell, M.A., Yeh, J.A. and Chiou, P.Y., 2016. Intracellular Delivery by Shape Anisotropic Magnetic Particle–Induced Cell Membrane Cuts. Journal of laboratory automation, 21(4), pp.548-556.

Chapter 1

Introduction

1.1 Demand for manipulation of biological objects

Manipulation of biological objects is vital in biomedical discipline that encompasses applications such as cells' or molecular interaction studies[1]–[4], single-cell analysis[5], [6], drug delivery[7], and tissue engineering[8], [9]. In the recent decades, the discipline has advanced rapidly due to the surge in demand for disease treatments, especially acute and chronic diseases for the aging population that is estimated to account for 16% of world population in 2050 as compared to 9% in 2019 (*World Population Prospects*[10]). Such demand drives the need for cell-based therapies, which often require an ability to facilitate the process of research and development in a well-controlled chemical micro-environment. That ability translates to what is known as manipulation of biological objects using lab-on-a-chip (LOC) technology, providing spatial control of cells in microfluids *in vitro*.

For cells' or molecular interaction studies, manipulation of micro-objects is essential to study the interaction responses. An example of cells' interaction study is the cell adhesion dynamics and actin cytoskeletal reorganization of neural and Hep2G hepatocarcinoma cells[4]. In order to carry out the investigation, the targets are

aggregated in a fluidic environment using a form of manipulation technique on LOC platform to facilitate the experiments. Another example of molecular interaction study is demonstrated by the Orwar group that succeeded in the recording of ion channel-ligand interaction by maneuvering ligands to the patch-clamped single cell on a LOC platform[3]. As claimed, the platform can also be utilized to enable characterization of weak-affinity receptor agonists/antagonists, bioactive molecules, etc. These examples reveal the importance of manipulation of biological objects.

Single-cell analysis is no exception. Deoxyribonucleic acid (DNA) damage and repair analysis, for instance, is performed by fixing a single cell onto a LOC device[5], offering the pathway for gel electrophoresis that lyses the cell to expose its DNA for assessment. Such device evaluates the efficacy of prospective cancer chemotherapeutics as inhibitors of human AP endonuclease, a DNA repair enzyme.

Drug delivery, too, relies on the manipulation technique using LOC technology. Lipid vesicles and polymeric nano- and microparticles have been prepared for drug delivery[7]. Stream of lipids in alcohol was hydrodynamically focused between sheathes of aqueous streams in micro-channel, allowing controlled mixing of the two streams that assembles the lipids into vesicles of tunable sizes. These vesicles are utilized to encapsulate micro-drugs.

In summary, the desire for manipulation of biological objects is great and the technological advancement to that manipulation ability is crucial in facilitating biomedical researches. Already, there are several physical mechanisms studied and devised on LOC devices; conventional examples include electrokinetic[11]–[13], acoustic[6], [14]–[29], optical[30]–[33], magnetic[30]–[33], and hydrodynamic[34]–[38] mechanisms. As

described in the following sections, each of these mechanisms has its advantages and disadvantages over one another.

1.2 Electrokinetic mechanism

Dielectrophoresis (DEP) is a phenomenon associated with electrokinetics, which enables transport of particles by induced polarization. Neutral particles are polarized by non-uniform electric field, where they experience the established field gradient that induces the DEP force for motion. The force can be approximated by the following expression[39]–[42]:

$$\vec{F}_{DEP} = 2\pi\varepsilon_1 \,\mathrm{Re}[K(\omega)] r^3 \nabla E^2 \qquad \textbf{1(a)}$$

where E is the electric field strength, r the particles' radius, and K the Clausius-Mossotti (CM) factor. Notice that the DEP force is proportional to the field intensity gradient, ∇E^2, which implies that the particles can be attracted toward or repelled from field minima or maxima. The direction of particles' movement is defined by

$$\mathrm{Re}[K] = \frac{\varepsilon_2^{\,*} - \varepsilon_1^{\,*}}{\varepsilon_2^{\,*} + 2\varepsilon_1^{\,*}} \qquad \varepsilon_1^{\,*} = \varepsilon_1 + \frac{\sigma_1}{j\omega} \qquad \varepsilon_2^{\,*} = \varepsilon_2 + \frac{\sigma_2}{j\omega} \qquad \textbf{1(b)}$$

where ω is the angular frequency of the electric field, ε and σ the dielectric permittivity and conductivity, and the subscript 1 and 2 denote surrounding media and particles, respectively. For positive Re[K] value, particles move toward the higher electric field gradient region, vice versa.

Based on the DEP principle, several LOC devices have been developed for patterning biological objects. An early example would be the Complementary Metal–

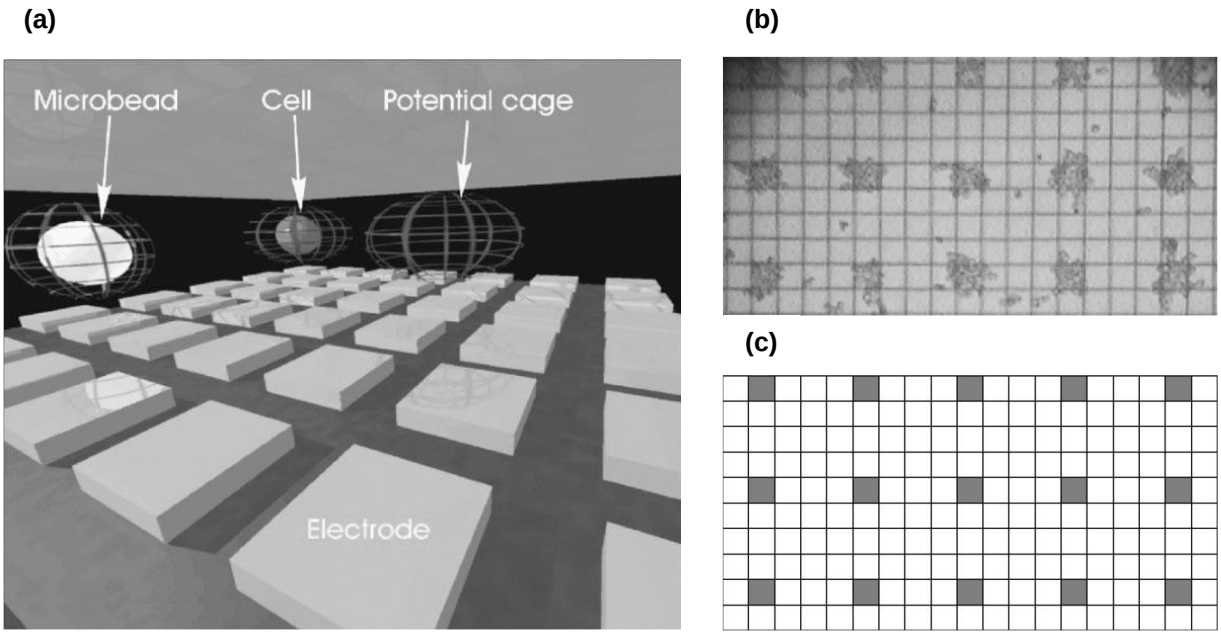

Figure 1.1 Schematic representation of a CMOS-based DEP device used for patterning micro-particles [42].

Oxide–Semiconductor (CMOS) chip used for manipulation of Saccharomyces cerevisiae[42], shown in **Figure 1.1**. An 8 X 8 mm^2 chip consisted of 102,400 actuation electrodes in array and fabricated using CMOS technology creates non-uniform electric field by adjusting the voltages applied to individual electrodes. As illustrated, electric potential cage, **Figure 1.1(a)**, can be generated to capture micro-beads and particles, **Figure 1.1(b)**, onto the target regions shaded in gray, **Figure 1.1(c)**. DEP manipulations are often conducted in low ionic isotonic buffers to maximize the forces for transport. However, isotonic buffers are not long term biocompatible and thus limits the DEP's applications. Although DEP manipulations in regular physiological buffers have been demonstrated, other issues such as electrolysis, heat generation, etc. need to be properly managed[43]. Electrolysis is the electrochemical reaction that occurs at the electrodes' surface and can hinder the device operation. Such reaction can be induced when operating at high voltage, particularly in highly conductive biological fluid, which is often

necessary to provide sufficient manipulation force. Additionally, local electrical damage due to high electrical field is harmful to biological samples and can induce cell lysis or significant local joule heating[44].

1.3 Acoustic mechanism

Acoustics is another physical mechanism used for manipulation of biological objects and has attracted a lot of research interests in recent decades for its superior biocompatibility and wide window of operable object' sizes. Past studies have shown biocompatibility in the MHz-order fields up to hours of operation[18], [45]–[47], and experiments have shown manipulation of objects sized from submicron scale to millimeter scale[6], [15], [18], [48]. In general, particles of different density and compressibility from the surrounding medium experience net acoustic radiation forces (ARF), incurred from non-uniform acoustic field distribution, that migrate them to either low or high potential energy regions. For particles of size much smaller than the wavelength (D<< λ), the ARF can be approximated by the following expressions[49]:

$$F^{rad} = -\nabla U^{rad} \quad \textbf{2(a)}$$

$$U^{rad} = \frac{4\pi}{3} a^3 \left[f_1 \frac{1}{2} \kappa_o < p^2 > - f_2 \frac{3}{4} \rho_o < v^2 > \right] \quad \textbf{2(b)}$$

$$f_1 = 1 - \frac{\kappa_p}{\kappa_0} \quad \textbf{2(c)}$$

$$f_2 = \frac{2(\frac{\rho_p}{\rho_0} - 1)}{2\frac{\rho_p}{\rho_0} + 1} \quad \textbf{2(d)}$$

where F^{rad} is the ARF, U^{rad} is the acoustic potential energy, a is the radius of particles, and p and v are the first-order acoustic pressure and velocity field at the particles'

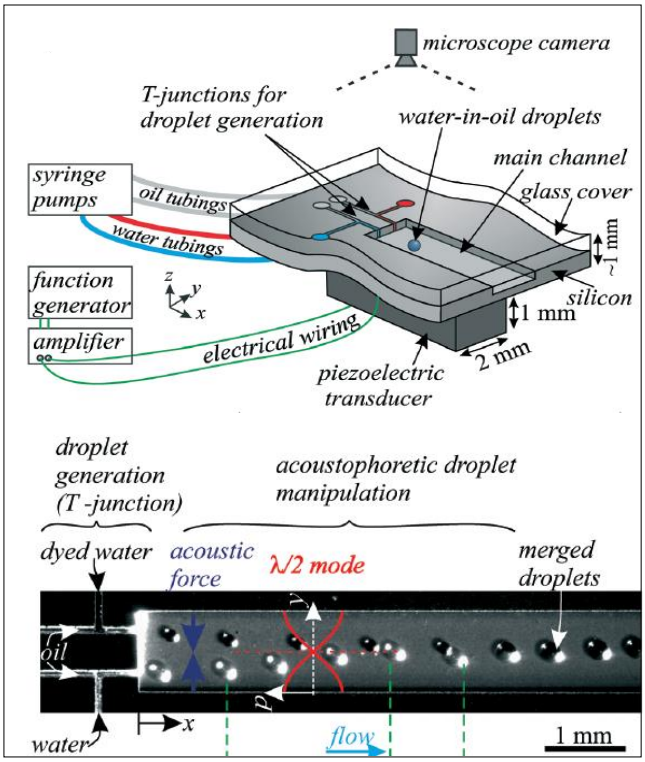

Figure 1.2 A Bulk Acoustic Waves (BAWs) device for merging water droplets sized in hundreds of micron[15].

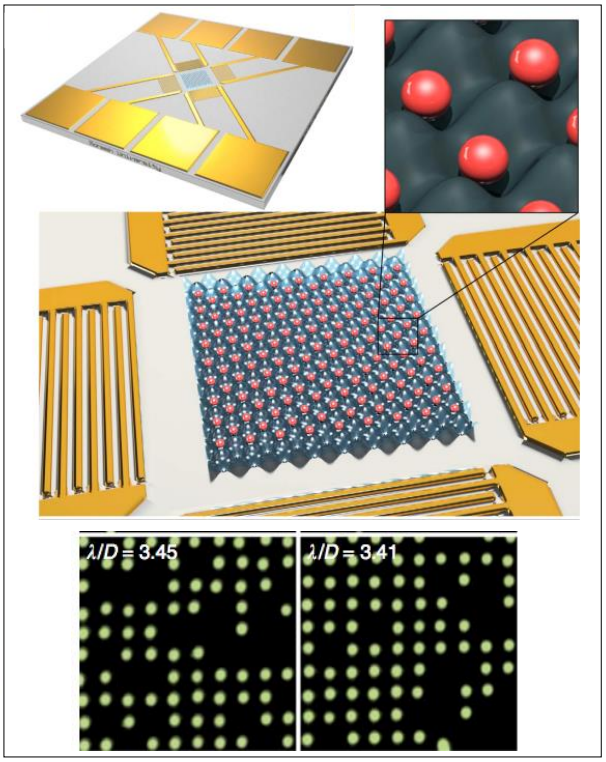

Figure 1.3 A Surface Acoustic Waves (SAWs) device for patterning micro-particles into a two-dimensional array[6].

location. The material compressibility κ and density ρ are subscripted by 'p' and 'o' for the particles and the surrounding medium, respectively.

Two frequently used acoustic mechanisms, bulk acoustic waves (BAWs)[14]–[17] and surface acoustic waves (SAWs)[6], [18]–[29], [50], have been applied to generate non-uniform acoustic field. In BAWs, acoustically hard structures, such as silicon or glass microfluidic chambers, are fabricated to form resonant cavities. Acoustic frequencies matching with certain acoustic modes of the cavities are chosen to excite standing waves in these structures to form the non-uniform field for which the waves are generated upon superpositioning of counter propagating waves. An example is illustrated in **Figure 1.2**, where a silicon channel is etched to the specified dimensions that create the standing waves with an acoustic mode of half the wavelength, $\lambda/2$. For this mode, the field non-

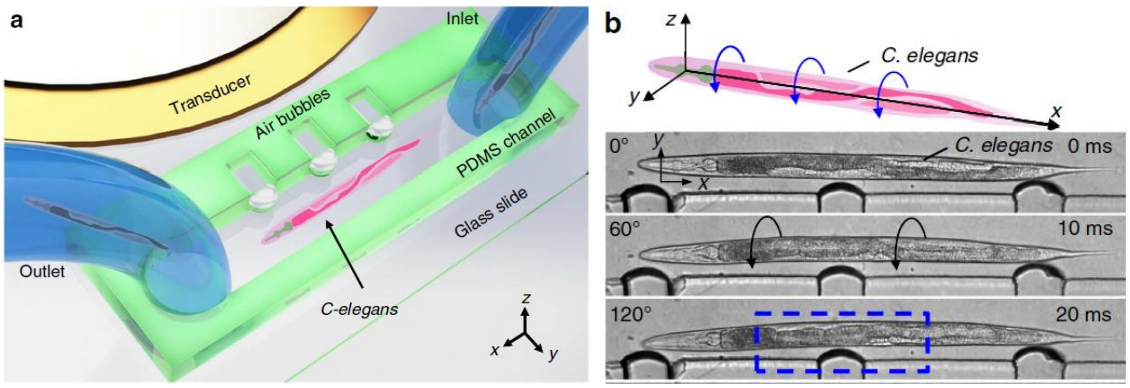

Figure 1.4 A SAWs device exploiting acoustic streaming force (ASF) in manipulating a C. elegans. Device schematics is shown (a), and its operating principle using air bubble's oscillation to rotate the object over an acoustic cycle is illustrated (b) [48].

uniformity is defined by its acoustic potential minima that occurs at the center of the channel which enables the oil-immersed water droplets to move and merge in the center line [15].

In SAWs, standing waves are generated by interdigitated transducers (IDTs) typically fabricated on a piezoelectric substrate, such as lithium niobate ($LiNbO_3$). **Figure 1.3** demonstrates such example of micro-objects patterning using IDTs. Two pairs of microfabricated IDTs perpendicular to each other generate the standing waves in 2-Dimension by superpositioning propagating travelling waves each originated from an IDT as shown, allowing the polystyrene micro-beads in water to be trapped in array of the acoustic potential wells formed. The IDTs are designed to operate at frequency as high as 185 MHz that corresponds to a wavelength of ~10 µm in water, creating sufficiently small sized acoustic wells where beads can be trapped individually. As results, an array of single-particle patterning is achieved[6].

An interesting example of objects manipulation using acoustic streaming force (ASF), rather than the ARF, is shown in **Figure 1.4**[48]. Acoustic streaming is a constant flow in fluid stemmed from the absorption of energy and momentum from the acoustic

oscillations[51]. This flow gives rise to the ASF which can be induced by exciting the air bubbles trapped in the grooves of the fluid-filled polydimethylsiloxane (PDMS) channel using the nearby transducer as the source of acoustic waves. This ASF is strong enough to rotate a C. elegans of sized ~1 mm in length, making acoustics a powerful mechanism to manipulate large biological object.

Nevertheless, the fundamental physics in using standing waves to create the non-uniform field confines the particles' patterning profile to be simple and periodic with a spatial resolution limited to half of the wavelength (1/2λ). For BAWs, resonant cavities are typically fabricated into rectangular shapes; due to the wave superposition relying on the cavities' wall reflections in the confinement that cannot be arranged into non-periodic shape, complex profile of acoustic potential cannot be induced. Although the shape of the cavities may be redesigned to resolve the issue, the attainable resolution is limited; for practical applications, BAWs devices operate in the MHz-regime which translates to the resolution in hundreds of micron in water, a size much larger than that of cells. For SAWs, due to the constrained SAWs-generation orientation, $LiNbO_3$ substrate prevents the creation of complex field distribution whose formation requires wave components of different frequencies and orientations. Although the field distribution can be manipulated to an extend by tuning the phases and frequencies of electrical signals applied to the IDTs, the achievable shape of patterned profile is still fundamentally limited. As demonstrated in **Figure 1.5**, SAWs are tuned by varying the phases, sequentially moving the position of acoustic potential wells, thus the trapped HeLa cells, to form the final alphabet patterns. However, not only such process of picking up and releasing cells one by one is slow but also is it not able to demonstrate pattern that is truly complex in

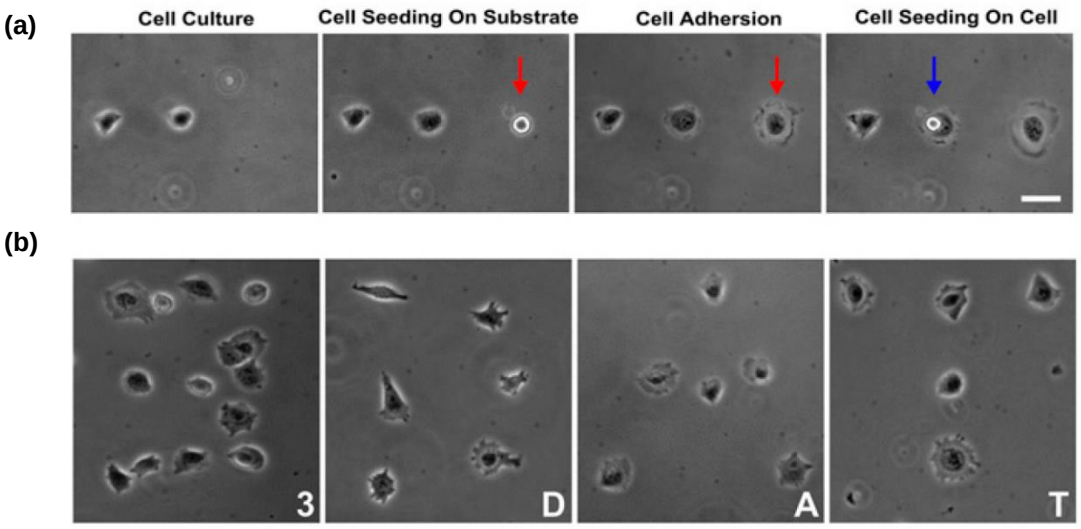

Figure 1.5 Sequential patternings of HeLa cells, achieved by varying the phases of applied electrical signals in a SAWs device, into a line shape (a) and letter shapes of "3", "D", "A", and "T"[20].

nature[20]. Holographic acoustic tweezers that use an acoustic hologram, or an array of sound emitters, can create complex patterns, yet, their spatial resolution is low[52], [53]. To improve the resolution, one must increase the acoustic frequency that adversely incurs significant heating due to high energy attenuation, potentially causing severe biocompatibility issue during manipulation of biological objects.

Despite that acoustic manipulation provides superior biocompatibility and wide range of operable biological object sizes, the current approaches cannot achieve high-resolution and re-configurable patterning in complex and non-periodic shapes. In this dissertation, we present the work in designing and developing a field-programmable acoustic platform, accomplishing two goals: (1) exploiting a new realm of acoustofluidics using a deep, sub-wavelength approach to facilitate high-resolution and complex patternings of micro-particles and (2) integrating a photothermal mechanism to allow not only versatile adjustment but also re-configuration to the potential energy profile.

1.4 Other physical mechanisms

On top of the electrokinetic and acoustic mechanisms, others such as optical, magnetic, and hydrodynamic mechanisms have also been applied for manipulating biological objects. However, optical mechanism is essentially limited by the conversion efficiency from optical into mechanical energy; moving cells in fluid can be a slow process. As results, large area operation will require extremely high optical power that is nearly impossible to generate. As for magnetic mechanism, biological samples do not usually show magnetic response, thus, requiring additional tagging or labeling of magnetic beads that could cause toxicity. Hydrodynamic mechanism is not without its disadvantage; the potential shear stress induced during the operation could rapture cells' membrane and cause damage[54]. In short, each of these mechanisms has limitations that prevent usage in practical application.

Chapter 2

Deep, sub-wavelength acoustic patterning of complex and non-periodic shapes on soft membranes supported by air cavities

2.1 Introduction

Cell manipulation *in vitro* is essential for many biomedical applications. Even though many physical mechanisms have been developed for cell manipulation using LOC devices, each of them has pros and cons in comparison. Among them, acoustic mechanism stands out for its superior biocompatibility and wide window of operable object sizes. Conventionally, standing waves technique is used to generate the non-uniform acoustic potential field needed to induce the ARF. However, such technique is limited to producing high-resolution, complex patterning shapes of objects. This is a setback to the technological advancement in cell manipulation in which the state-of-the-art technology lacks both the superiority in biocompatibility and complex shape patterning capability altogether.

Here, we designed and fabricated an acoustic device platform exploiting deep, sub-wavelength patterning technique, a new realm within acoustofluidics that has not yet been explored. To realize the approach, we developed an air-embedded, viscoelastic structure made of PDMS. The embedded air cavities are designed to have sizes smaller than half the wavelength. Since air has acoustic impedance ~10000 times less than that

of most materials[55], majority of the acoustic waves will not be able to pass through the interface between air and other materials. This creates voids, or acoustic potential wells, within the space of acoustic wavefront on the other side of the interface. A crucial novelty behind such sub-wavelength approach is that the acoustic wells can be generated easily into complex shapes because their geometry follows that of the air cavities. Following this design concept, we have succeeded in complex and non-periodic patternings of biological objects.

2.2 Device operation principle

We name the newly developed acoustic platform “Complaint Membrane Acoustic Patterning”, or CMAP. This platform allows creation of complex and non-periodic acoustic potential wells at deep, sub-wavelength scale. The potential landscape can be realized by exciting acoustic traveling waves, generated using a piezoelectric ceramic PZT (lead zirconate titanate), to pass through desired shapes of air cavities embedded in a soft, viscoelastic PDMS structure, as illustrated in **Figure 2.1**, that have sizes much smaller than the wavelength. PDMS is chosen since its acoustic impedance is close to that of surrounding fluid (e.g. water) for which the wave reflections at the PDMS/water interface can be minimized[56]. Air is utilized since it has large acoustic impedance difference to most materials for which majority of the waves can be reflected[57], [58]. As results, near-field acoustic wells are formed immediately above the air cavities with a spatial resolution matching to the cavities’ size. A thick PDMS layer atop the water layer serves as a wave-absorbing medium to prevent acoustic waves from reflecting.

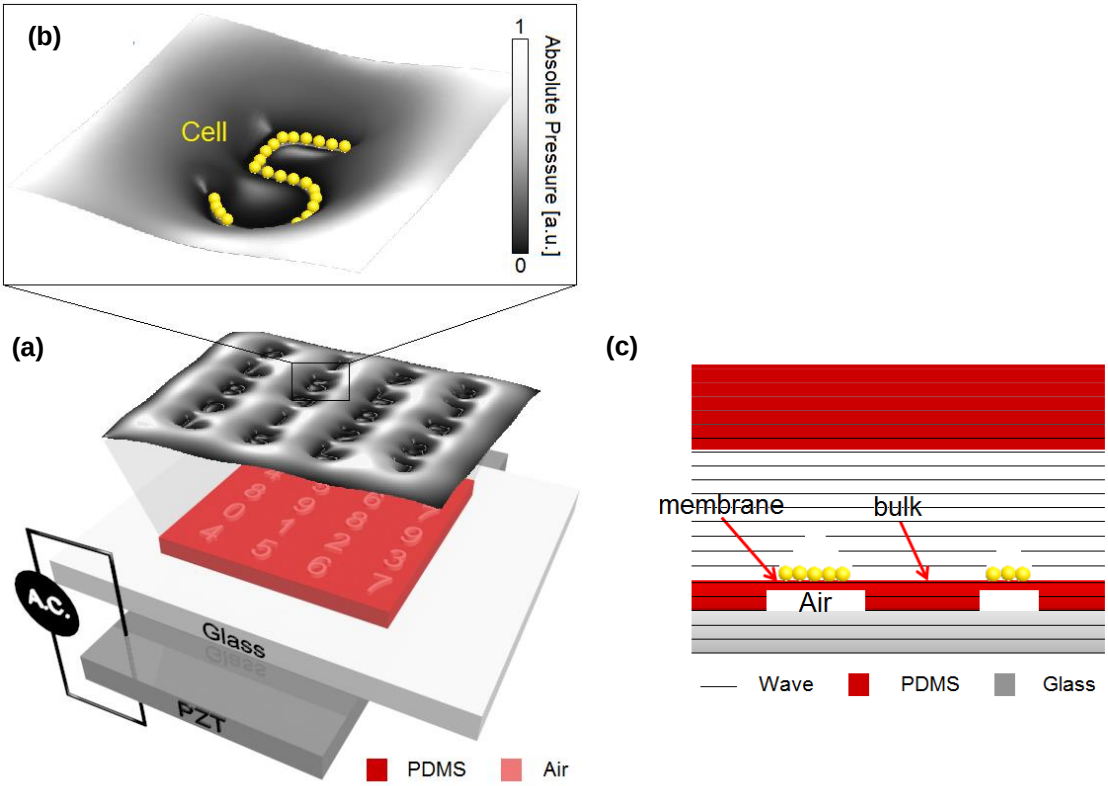

Figure 2.1 CMAP device platform that enables complex shaped, deep sub-wavelength patterning of micro-particles. (a) The device platform consists of a PZT substrate as the power source, a glass intermediate allowing re-attachment of the above air-embedded PDMS structure, and the PDMS structure that selectively blocks incoming acoustic travelling waves using air cavities. (b) A representative schematic of the resulting acoustic radiation potential field immediately above the PDMS structure is shown. (c) Cross-sectional view of the platform shows the bulk and membrane regions of the PDMS structure, as well as a PDMS encapsulation.

One major challenge encountered in conventional acoustic patternings is the coupled fluid and structure vibration that complicates the design of device structure. With the CMAP platform, we can minimize the effect of structure-induced vibration that would otherwise interfere the intended acoustic field and, ultimately, able to predict the shape of particle patterning by using a simple pressure wave propagation model. This innovation is carried out by incorporating a thin and compliant, viscoelastic PDMS membrane to interface the air cavities and the above chamber fluid. When the pressure waves propagate through the air-embedded PDMS structure, the vibration in the bulk decays within a short distance into the membrane due to two primary characteristics. One

characteristic is the membrane's thinness and compliance for which it does not have sufficient stiffness to drive and move the fluid mass atop at high frequency. The second characteristic stems from material damping of the structure at high frequency that prevents the vibration energy from building up in the membrane region. Thus, the fluid pressure above the membrane region does not fluctuate much with the waves that propagate through the bulk into the fluid and remains at a relatively constant level compared to regions in the bulk. This creates a low acoustic pressure zone above the membrane and establishes a pressure gradient between the bulk and membrane regions. Since this near-field pressure zone depends on the membrane area attained from the air cavities that can be fabricated into any size and geometry, complex and non-periodic patterning of micro-particles with a spatial resolution much smaller than the wavelength can be realized.

Additionally, large area patterning can be achieved using the same actuation principle. For the fact that PZT substrate generates plane acoustic waves with uniform intensity, the maximum operating area is only limited by the PZT's available size. In short, since the acoustic potential landscape of CMAP platform does not rely on the formation of standing waves and since the disturbance to the landscape due to the structure-induced vibration may be minimized, the shape of potential wells simply reflects that of the air cavities.

2.3 Device characterization through finite element analysis (FEA) simulation

To quantitatively understand the CMAP operation principle, we study the relationship between the material properties of PDMS and their effects on structure-

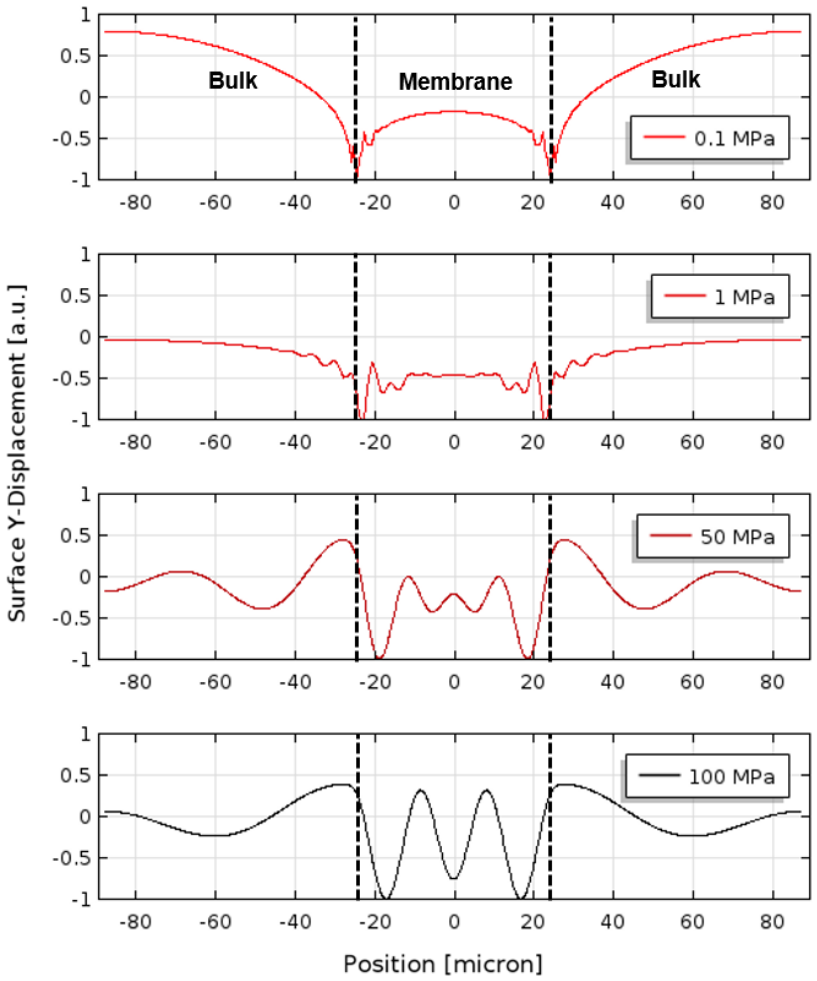

Figure 2.2 Acoustic-structure interaction simulations investigating the effect of changing material properties of the air-embedded PDMS structure. During vibration, the surface of the PDMS structure interfacing the chamber fluid shows smoother profile and lower order structure vibration mode when the E' of the structure decreases from 100 MPa to 0.1 MPa. This is especially noticeable at the membrane region.

induced vibration using numerical simulation. Finite element (F.E.) solver COMSOL Multiphysics 5.3 with acoustic-structure interaction module is implemented, as shown in **Figure 2.2**, to study the acoustic potential landscape as the result of the soft/hard, air-embedded PDMS structure interacting with the chamber fluid upon excitation. The relationship $\eta_s = E''/E'$, where E' is the dynamic storage modulus, E'' is the dynamic loss modulus, and η_s is the isotropic loss factor of the PDMS structure accounting for the structural damping, is explored under the sinusoidal excitation frequency at 3 MHz. The

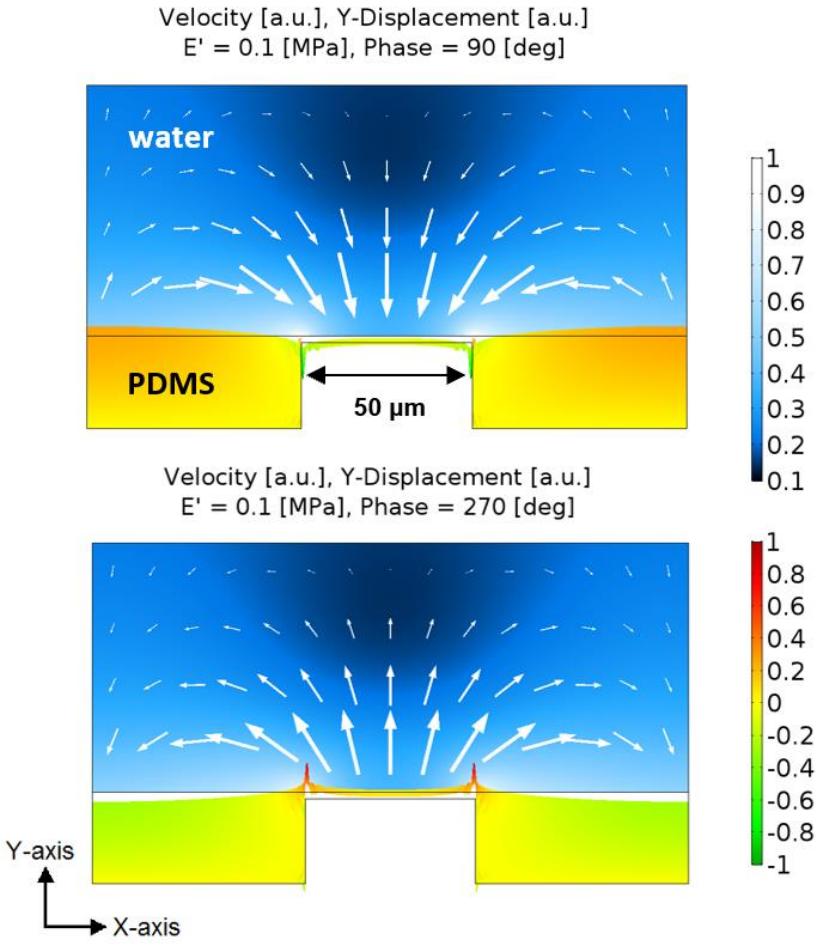

Figure 2.3 Acoustic-structure interaction simulations investigating the effect of changing material properties of the PDMS structure on the chamber's fluid. A low E' gives rise to the compliance of membrane to the above fluid such that upward displacement of fluid above the bulk drives the fluid towards the downward, deforming membrane, vice versa.

model geometry, **Figure 2.3**, considers a 50 µm wide air cavity embedded in a solid structure that leaves a 2 µm suspended membrane interfacing an above incompressible fluid. As such, we simulated the solid structure and fluid to represent the PDMS and water, respectively. The bottom boundaries of the structure are excited using a prescribed displacement in y-direction, simulating the mode of vibration of the PZT along its thickness. For simplicity, η_s is assumed to be constant (0.2), while the moduli are varied. The resulting total acoustic pressure in the fluid is then calculated by the F.E. solver, which solves the acoustic-structure interaction at the interface between the fluid and

structure, as well as the inviscid momentum conservation equation (Euler's equation) and mass conservation equation (continuity equation) in the fluid. The simulation assumes classical pressure acoustics with isentropic thermodynamic processes and assumes time-harmonic wave. For a harmonic acoustic field, $v_{in} = \frac{1}{i\omega\rho_0}\nabla p_{in}$, where ω is the angular frequency in rad/s. The simulation not only allows post-processing of the acoustic potential landscape generated (**Figure 2.4a** and **2.4b**) using **Equation 2b**, but also enables studies of 1st order velocity of the chamber fluid (**Figure 2.3**) and surface profile of the solid (**Figure 2.2**) as function of E' and membrane size, respectively.

The result, **Figure 2.2**, examines the vertical displacement of the PDMS structure's surface interfacing the fluid. Strong membrane vibration is observed for the structure of high E' at 100 MPa. This opposes to the case of low E' at 0.1 MPa in which the structure-induced vibration from the bulk decays substantially in a short distance at the membrane edge, leaving the membrane to be relatively flat and smooth. The softness and lightness of the membrane enable it to follow the motion of water when cycling through different phases of the excitation (**Figure 2.3**). Under an ideal operation condition, as acoustic waves travel through the patterned PDMS structure, the surface oscillation motions of the membrane and the bulk should be in the opposite direction, or out of phase. When the water above the bulk is being displaced upwards at phase 90 deg., the developed pressure drives the water towards the downward, deforming membrane to satisfy mass conservation ($\nabla \cdot V = 0$) since it occurs on a length scale much shorter than the acoustic wavelength ($d \ll \lambda$). When the water above the bulk moves downwards at phase 270 deg., the water atop the membrane flows back to the bulk region. These back-and-forth fluid motions are repeated under the sinusoidal excitation.

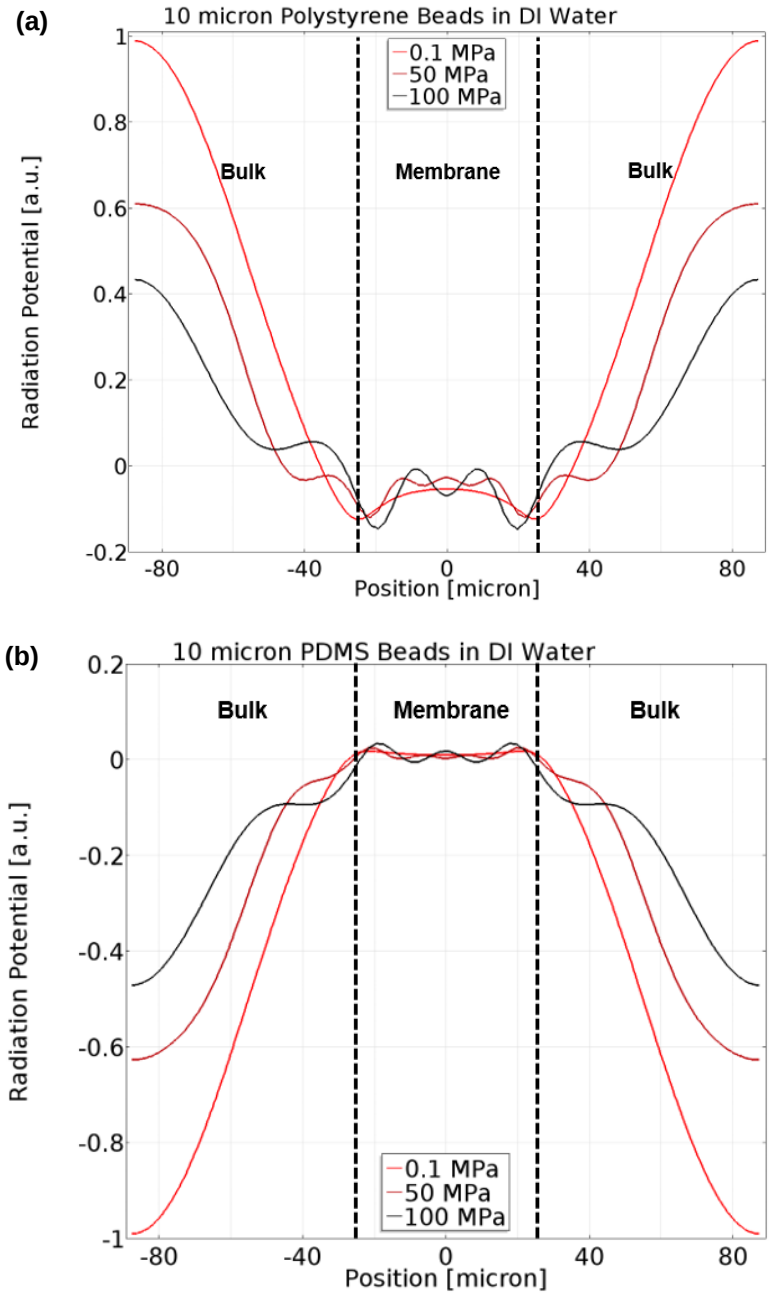

Figure 2.4 Acoustic-structure interaction simulations investigating the effect of changing material properties of the PDMS structure on the radiation potential of particles. The resulting acoustic potential landscapes, 5 µm above the PDMS structure, for 10 µm polystyrene beads (a) and 10 µm PDMS beads (b) in water are simulated. For the polystyrene beads, high E' creates multiple potential wells across both the bulk and membrane regions while low E' creates potential wells conforming to the membrane area; notice that all the minimum potential wells are generated at the membrane edges. On the contrary, PDMS beads with higher compressibility revert the potential profiles.

Acoustic radiation potential landscape is estimated by accounting the resulting water pressure and velocity fields near the PDMS-fluid interface into **Equation 2(b)**. For

10 μm polystyrene beads ($\rho_p = 1050\ kg\ m^{-3}, \kappa_p = 2.38 \times 10^{-10} Pa^{-1}$)[59], [60], the potential profile at 5 μm above the air-embedded PDMS structure of E' at 100 MPa, **Figure 2.4**, reveals strong variation that leads to multiple metastable wells across both the membrane and bulk. On the other hand, the potential profile for the structure of E' at 0.1 MPa shows much smoother landscape with wells generated only at the membrane region, enabling beads' patterning shape that conforms to that of the air cavity. Minimum potential wells occurred at the membrane edges rather than at the center because the perturbed pressure term in **Equation 2(b)** is weak and the velocity term dominates at these regions. The relative contributions of the pressure and velocity terms in the potential profile can be better explained by the energy density plots, $\frac{1}{2}\kappa_o < p^2 >$ and -$\frac{3}{4}\rho_o < v^2 >$, in **Figure 2.5** and their multiplication with the particle property factors ($f_1 = 0.465$ and $f_2 = 0.032$ for polystyrene beads in water). The large f_1 factor, compared to f_2, allows the pressure term to dominate in most regions except at the membrane. The fluctuation of the potential profiles at the membrane region in **Figure 2.4(a)** is primarily attributed by the velocity term. Nevertheless, from the potential profile simulated for the case of structure of E' at 0.1 MPa, it can be predicted that the beads will begin accumulating at the membrane edges then eventually moving toward the center as more beads fill in from the bulk.

Contrarily, for PDMS beads ($\rho_p = 965\ kg\ m^{-3}, \kappa_p = 8.95 \times 10^{-10} Pa^{-1}, f_1 = -1.011, f_2 = -0.024$) that exhibit greater compressibility than water, the compressibility reverts the profiles of **Figure 2.4(a)** which leads to trapping of the beads at high-pressure regions outside the air cavity as illustrated in the simulated results in **Figure 2.4(b)**. In addition, it has been shown that the speed of sound of PDMS can drop rapidly from ~1000

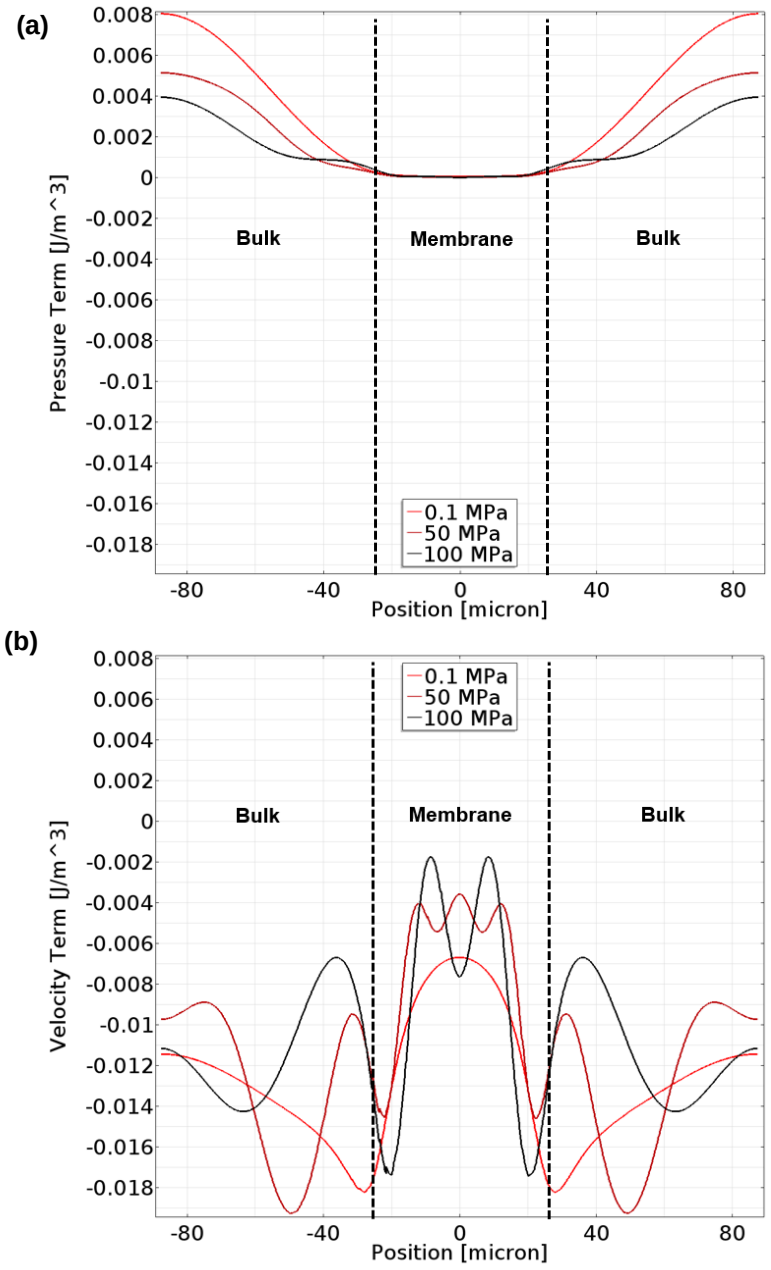

Figure 2.5 Analysis of the contributing factors to the resulted acoustic potential profile of Figure 2.4(a). The pressure term $\frac{1}{2}\kappa_o < p^2 >$ **(a)** of the radiation potential **Equation 2(b)** shows same trend across the entire range of E' examined such that the pressure decreases from the maximum outside the membrane region to the minimum at the center. On the other hand, the velocity term $-\frac{3}{4}\rho_o < v^2 >$ **(b)** of **Equation 2(b)** shows variations across the range of E', except at the edges of membrane region where largest amplitude occurs. The higher the E' is the stronger the fluctuation of the velocity term becomes. In all cases, largest velocity amplitude occurs at the membrane edges.

m/s to ~40 m/s when the porosity varies from 0 to 30%[61]. Based on the relationship $\kappa_p = 1/\rho c^2$, where c is the speed of sound, the high compressibility of porous PDMS can

result in a f_1 factor orders of magnitude larger than f_2, making the pressure term to further dominate.

As simulated, the compliant, viscoelastic PDMS membrane effectively limits the structure-induced vibration propagating from the bulk into the membrane region. This unique feature permits membranes of sizes larger than the propagation length to be utilized for complex and non-periodic patterning on CMAP. In **Figure 2.6**, the vibration from the bulk decays in ~10 μm from the edges of the PDMS membrane (E' at 0.1 MPa), regardless of the membrane width. In other words, the design process to create a desired potential landscape is greatly simplified via bypassing the complicated analysis of fluid-structure interaction and acoustic modes encountered in the conventional acoustic devices.

2.4 Device fabrication and assembly

To evaluate the acoustic-structure interaction simulation, we fabricated the CMAP device platform and tested it experimentally. In details, the CMAP platform, **Figure 2.1**, consists of a PZT substrate (lead zirconate titanate), soda-lime glass, and top and bottom PDMS structures. The PZT of dimension 3 cm × 1 cm × 0.05 cm (L × W × H) from APC International Ltd. and of material type 841 generates acoustic travelling waves across the device. On the top, a soda-lime glass slide from Corning (Model 2947-75x50) dimensioned 2 cm × 2 cm × 0.1 cm (L × W × H) is affixed using epoxy. Glass allows easy re-attachment of the air-embedded PDMS structure which renders the PZT substrate to be reusable.

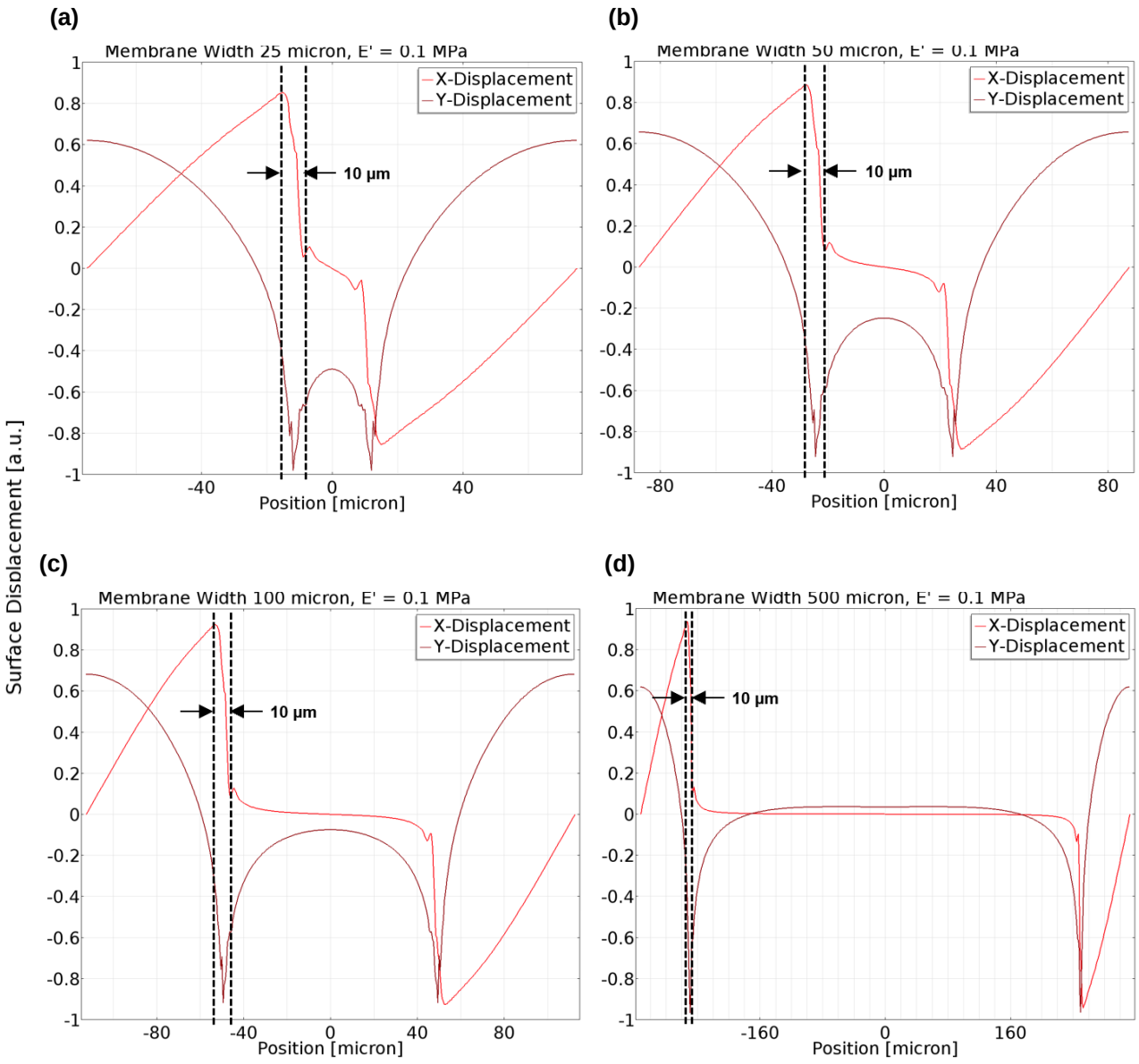

Figure 2.6 Simulated surface displacements of soft, air-embedded PDMS structure with varying air cavity widths. To determine the length of wave decay from the bulk into the membrane region, we explore different widths of air cavity sized from 25 μm to 500 μm **(a-d),** assuming the structure of E' of 0.1 MPa, following the simulation model in **Figure 2.3**. Results show that, regardless of the membrane sizes, wave propagating from the bulk decays in ~10 μm.

For testing, we fabricated two types of CMAP platform by synthesizing each with different PDMS Young's Moduli, E, to form the air-embedded, viscoelastic structure; hard and soft types. The hard, air-embedded PDMS structure is fabricated, in a similar fashion as the standard PDMS replica molding[62] following the manufacturer's instructions using

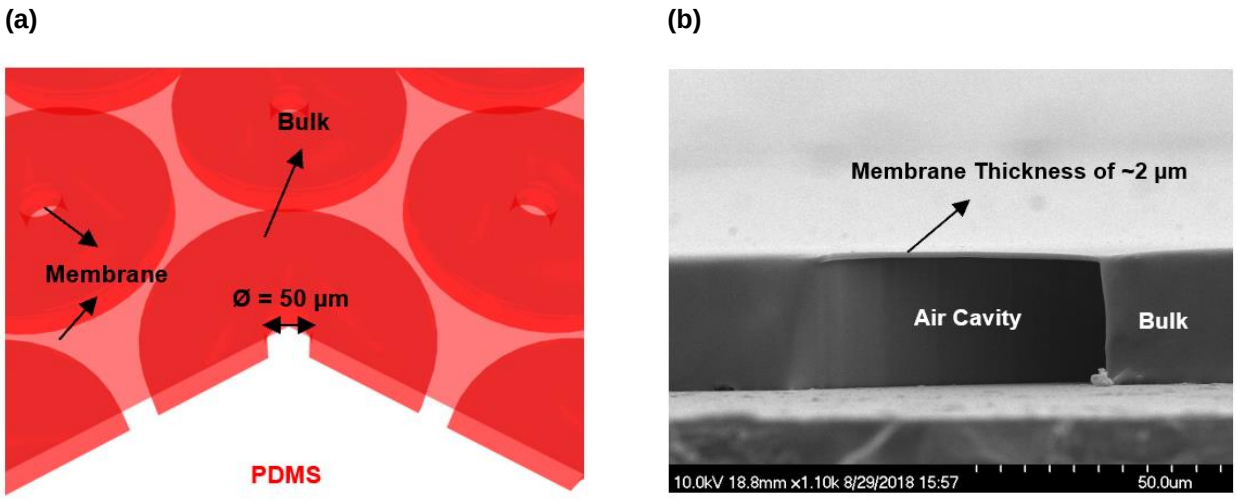

Figure 2.7 Sample illustration of soft, air-embedded PDMS structure in concentric rings-shape. Model geometry is shown in **(a),** accompanied by a fabricated sample's SEM image in cross section revealing the suspending PDMS membrane **(b)**.

Sylgard 184 (Dow Corning Co.), producing E of ~1750 kPa[63]. The master mold is composed of MicroChem Corp's SU-8 3025 micro-structures photolithography-patterned on a Silicon wafer which shapes the embedded air cavities. The molding process is carried out by covering the master mold in the Sylgard 184, stamping the mold using another slide of glass topped with aluminum block (~7,500 g), and cured in an oven at 70^{o}C for 4 hours. For the soft PDMS structure also demonstrated in the experiments, molding process differs by using a mixture of Sylgard 527 (Dow Corning Co.) and 184 in a weight-to-weight ratio of 4 to 1, producing E of ~250 kPa[63]. Curing of such mixture is performed at room temperature. As resulted from the molding process, an approximately 2 µm thick of meniscus is formed on the micro-structures and it becomes the PDMS membrane (see an example of the model geometry, **Figure 2.7(a)**, of a PDMS structure in concentric rings-shape). In determining the thickness of the membrane, the fabricated PDMS structures are cut to reveal the cross section (see the Scanning Electron Microscopy, SEM, image of the fabricated PDMS membrane's cross section, **Figure**

2.7(b))., and 3 membranes are examined using SEM. The measured thicknesses are 1.09 µm, 1.14 µm, and 1.33 µm, and their average thickness is approximately 2.18 µm. For simplicity, we assume a 2 µm membrane thickness to be used in our simulations. Subsequently, the hard/soft PDMS structure is transferred onto the device's glass layer.

Micro-particles, or biological micro-objects, are then pipetted onto the PDMS structure and encapsulated with another layer of thick PDMS. To minimize wave reflection inside the device's chamber, PDMS of Sylgard 184 is used as the encapsulation for its close acoustic impedance to that of water. In addition, the thickness of the encapsulation is designed to be 1 cm, which enables sufficient wave energy attenuation at our operating frequency of 3 MHz to prevent reflection from the interface between ambient air and device[64], [65].

2.5 Device setup and operation

The complete experimental setup, **Figure 2.8**, to using the CMAP device platform involves a power amplifier (ENI Model 2100L), a function generator (Agilent Model 33220A), a T.E. cooler (T.E. Technology Model CP-031HT), an ultra-long working distance microscope lens (20× Mitutoyo Plan Apo), and a recording camera (Zeiss Model AxioCam mRm) mounted onto an upright microscope (Zeiss Model Axioskop 2 FS). Surfaces of the PZT are wire-bonded and electrically connected to the power amplifier that is controlled by the function generator to feed the A.C. signals. Upon receiving the signals, the PZT transforms the sinusoidal voltages into mechanical vibrations to generate the acoustic traveling waves across the device. Additionally, to prevent cell damage from excessive PZT heating, we operated the device on a T.E. cooler set at 12°C for all

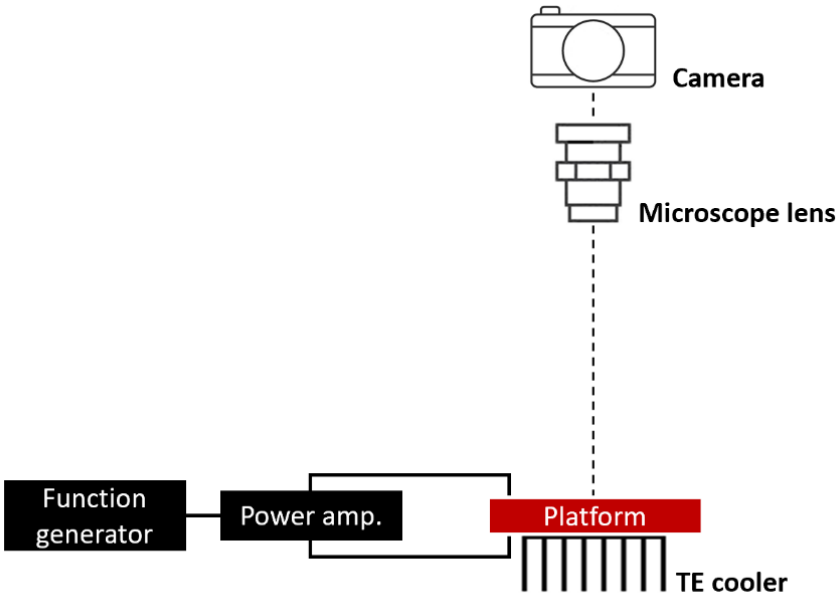

Figure 2.8 Experimental setup of the device platform.

experiments. To monitor the temperature of the device's chamber, we inserted a thermocouple (Omega OM-74) through the PDMS encapsulation and reran the experiment with only water in the chamber; result shows stabilization below the incubation temperature of 37°C, suggesting suitability for long-term operation. The entire device platform is positioned under the Mitutoyo microscope lens. Patterning process is then observed through the PDMS encapsulation that allows clear visualization and is recorded using the accompanied Zeiss AxioCam.

2.6 Device characterization using Laser Doppler Vibrometer (LDV)

Hard and soft, air-embedded PDMS structures are fabricated using the respective mixture of Sylgards and are molded into arrays of concentric rings-shape as shown in **Figure 2.7**. Their surfaces are then characterized using LDV. Note that although E_s

mentioned previously are static moduli, decrease in E is accompanied by decrease in both the dynamic moduli, E' and E''[66]. Hence, the two compositions became the hard and soft structures representing the prior simulated cases of E' at 100 MPa and 0.1 MPa, respectively. For the characterization, the PDMS structures are integrated into the CMAP device plafform and are driven at similar operation conditions to those set in the simulations. As illustrated in **Figure 2.9(a)** and **(b),** the surface vertical displacements of the hard and soft PDMS structures are measured over a cycle of acoustic excitation. **Video 1** and **2** in the supplementary materials also demonstrate the structures' LDV measurements over the cycle. For the hard structure, the surface profiles at phase 90 and 270 deg. show structural perturbation that propagates deeply into the center of membrane which excites high-order structure vibration mode, resembling the simulation results for E' at 50-100 MPa, **Figure 2.2**. For the soft structure at the same phases however, the displacement profiles at the center of membrane are smooth and resemble those of simulated E'at the range between 0.1-1 MPa, **Figure 2.2**. In short, the results of the characterization using LDV matches those of the simulations, thus, we expect the patterning profiles of particles would follow closely to the shape of simulated acoustic potential profiles. Of note here is that, in addition to the difference between the dynamic and static moduli, variation in PDMS thickness could modify its mechanical properties[67].

2.7 Experimental demonstration of complex and non-periodic patternings of micro-particles

Complex and non-periodic patterning of particles has been a major complication in the field of acoustofluidics, where the patterning resolution and profile are restricted by

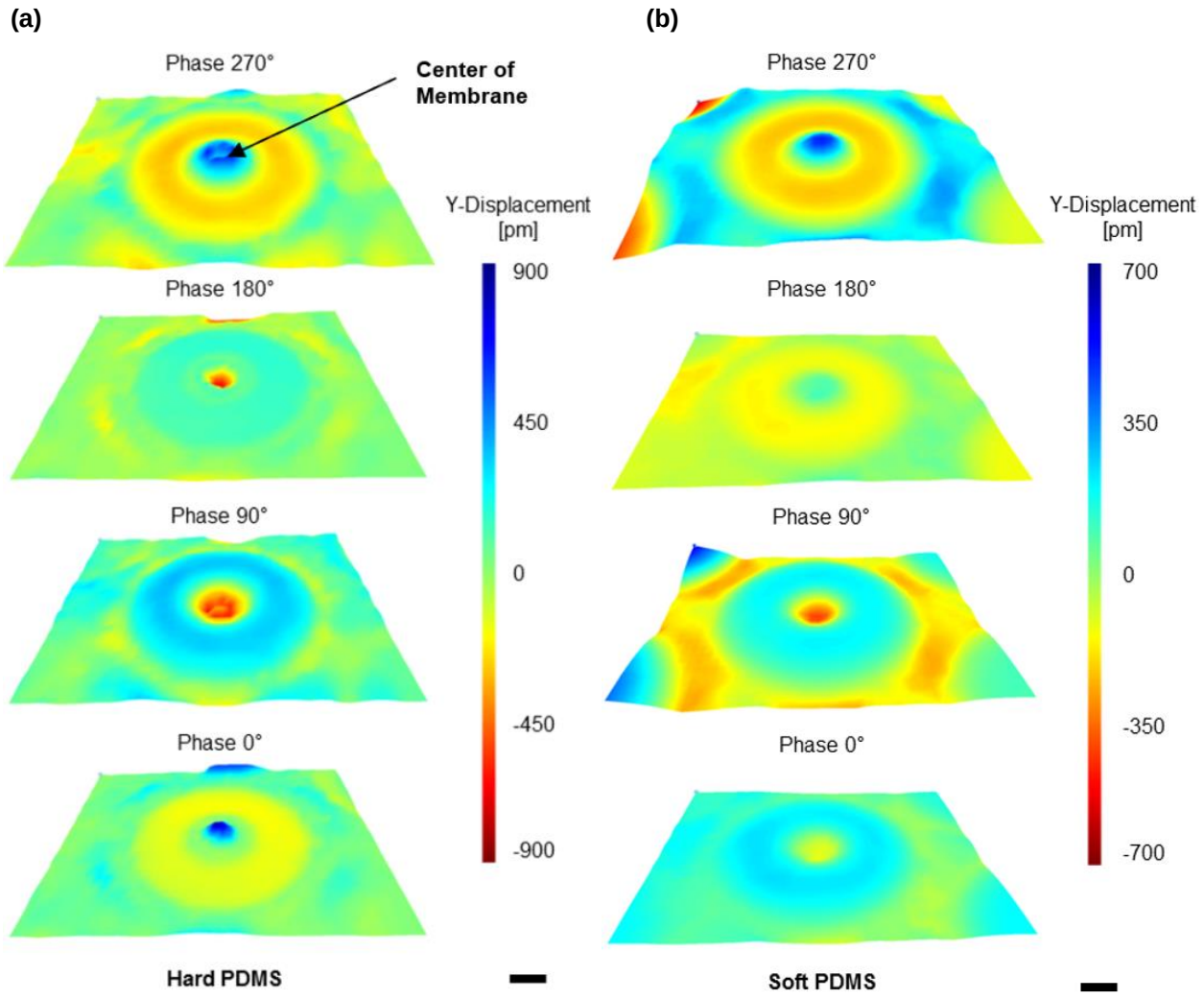

Figure 2.9 LDV measurements of the vertical surface displacement of hard and soft, air-embedded PDMS structures cycling through different phases of a sinusoidal excitation at 3MHz. The hard and soft PDMS of high and low E', respectively, exhibiting varying surface vibration patterns are demonstrated using the concentric rings-structure shown in **Figure 2.7**. During the excitation, the surface profiles between the two PDMS structures **(a)** and **(b)** are noticeably different at the center membrane. Not only the hard PDMS structure generates higher order structure vibration mode but also creates larger area of membrane vibration relatively to the bulk. Scale bar, 50 µm.

attainable wavelength size and limited, periodic acoustic potential landscapes, respectively. Alternatively, the new acoustic patterning mechanism using the CMAP approach allows us to overcome these challenges. As demonstrated in **Figure 2.10**, 10 µm polystyrene beads (fluorescent green polystyrene beads from Thermo Fisher Scientific) in water are patterned using the prior hard and soft, air-embedded PDMS

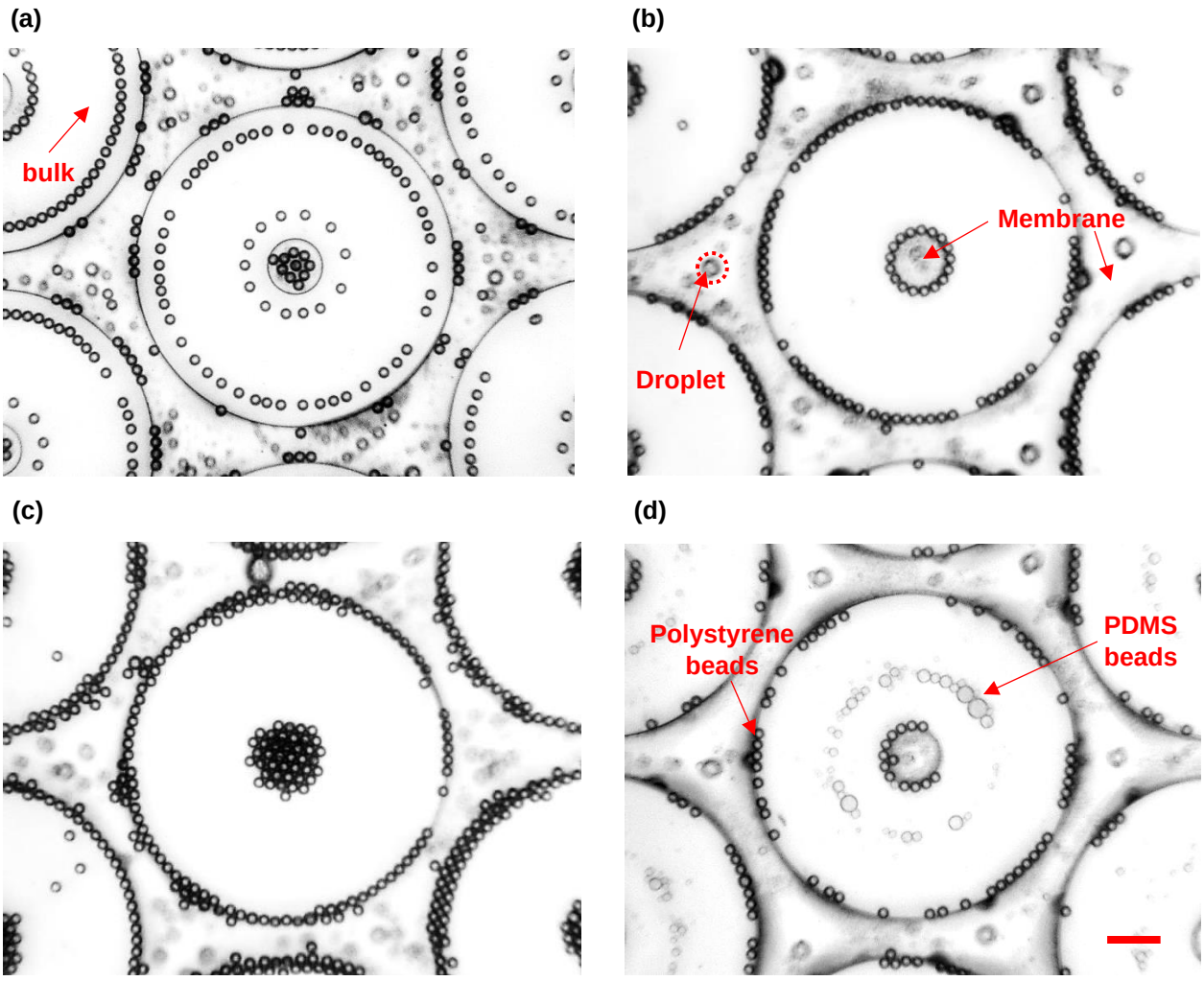

Figure 2.10 Patternings of micro-particles in water using hard and soft, air-embedded PDMS structures in the shape of concentric rings. Hard and soft PDMS compositions are used to fabricate the concentric rings structures for comparison. Hard PDMS structure (**a**) leads to multiple patterns of 10 µm polystyrene beads across the bulk and membrane regions. Soft PDMS structure (**b, c**) enables clean patterning profiles precisely following the shape of air cavities. In low concentration (**b**), the beads are aligned with the edges of membranes where the lowest potential wells reside. In high concentration (**c**), the beads initially trapped at the edges were pushed into the membrane region where there are more beads than what the edges can hold. In a mixture (**d**), polystyrene and PDMS beads migrate to the locations of low and high pressure, respectively, corresponding to the potential landscapes simulated in **Figure 2.4**. Notice that water droplets are formed beneath the suspended membranes. Scale bar, 50 µm.

concentric rings-structures at the operating frequency of 3 MHz and voltage of 5 V_{rms}. While both structures demonstrate patternings that conform to the shape of membranes/air cavities, the hard PDMS structure in **Figure 2.10(a)** exhibits additional trapping profile in the bulk region. This is exemplified by the simulation, **Figure 2.4(a)**,

that the PDMS structure of high E' at 100 MPa creates extra metastable potential wells in the bulk region. Both the experimental and simulation results show additional wells generated ~20 μm away from the membrane edges. On the contrary, the soft PDMS structures in **Figure 2.10(b)-(d)** show trapping profiles only at the membrane edges. For the simulated PDMS structure of low E' at 0.1 MPa, **Figure 2.4(a)**, effective damping of wave propagation into the membrane provides membrane compliance to the above fluid motion where, and only where, the potential wells are generated. In low concentration of beads, **Figure 2.10(b)** and **Video 3** in the supplementary materials, trapping began at the membrane edges, where the lowest acoustic potentials reside as explained before. Such trapping was realized over a repeated concentric rings-pattern spanning over a 3 × 3 mm^2.

Furthermore, as observed from the lining of the beads between the neighboring rings, a spatial resolution of 50 μm has been achieved, which is 10 times lower than the applied acoustic wavelength (~500 μm). This indicates the subwavelength resolution capability of CMAP as compared to other conventional acoustic approaches; **Figure 2.11(a)-(c) and 2.11(d)-(f)** further demonstrate the capability using soft, air-embedded PDMS stripped and circular-structures, respectively, spaced at 20 μm, 50 μm, and 100 μm apart, and the results confirm to the 50 μm spatial resolution achieved. At higher concentration, **Figure 2.10(c)**, beads initially trapped on the edges of membrane are pushed toward the center, thus filling up the entire membrane space. Patterning of the mixture of polystyrene and PDMS beads, **Figure 2.10(d)**, is also demonstrated; result confirms to the simulations that the PDMS beads would accumulate at the high-pressure region in contrary to the polystyrene beads. This contrast reflects CMAP's potential applications such as particle sorting and visualization of acoustic waves[68]–[70]. In the

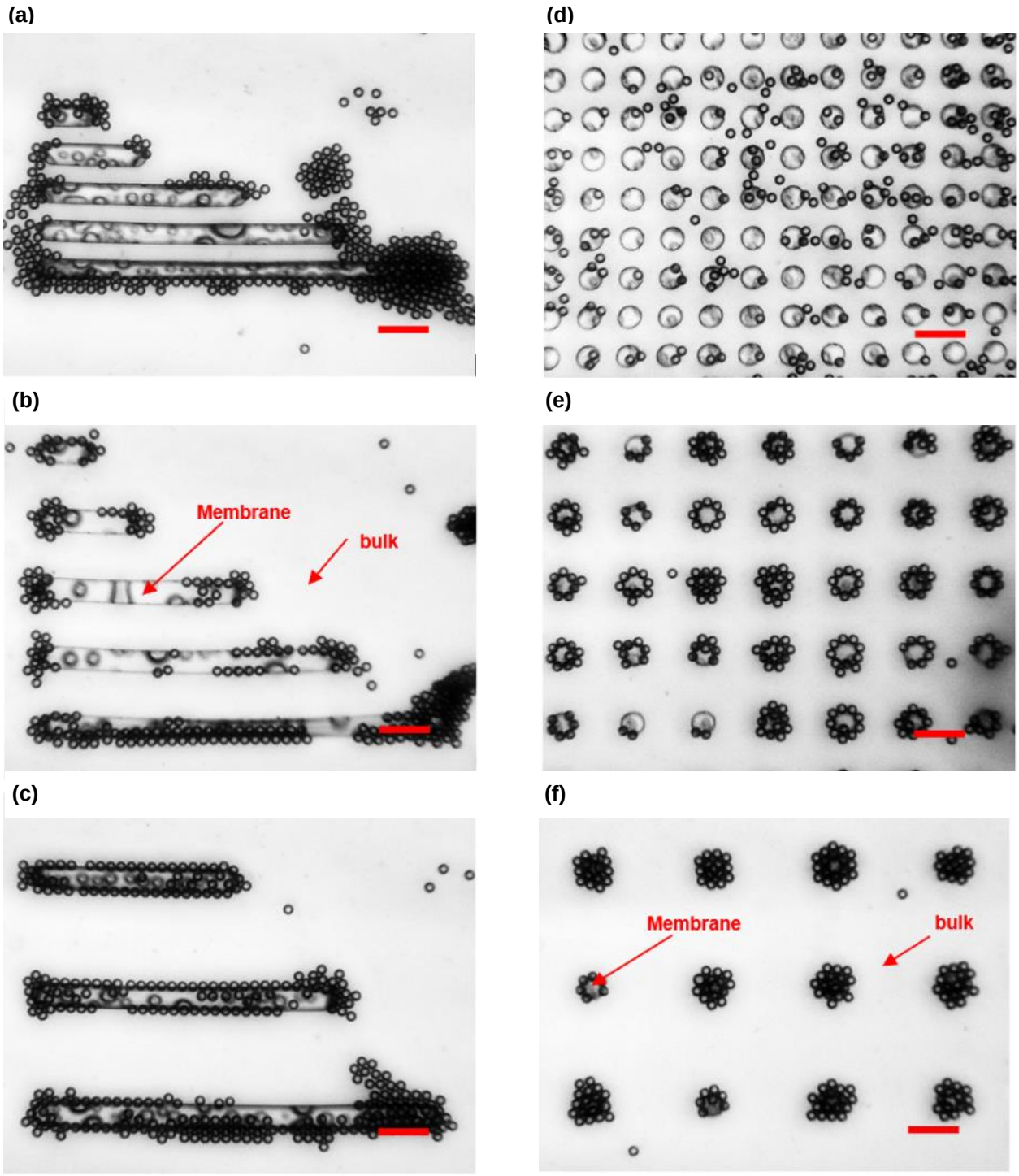

Figure 2.11 Patternings of micro-particles in water using soft, air-embedded PDMS structures in the shape of strip and circle. Under 3 MHz excitation, stripped-structures spaced at 25 µm (A), 50 µm (B), and 100 µm (C) are used to pattern 10 µm polystyrene beads. Results show trapping distortion at 20 µm spacing, indicating the CMAP's resolution at 50 µm. Equivalently, patterning using circular-structures spaced at 25 µm (D), 50 µm (E), and 100 µm (F) show the best resolution at 50 µm. Scale bar, 50 µm.

future, CMAP may be redesigned to include soft, air-embedded PDMS structures of

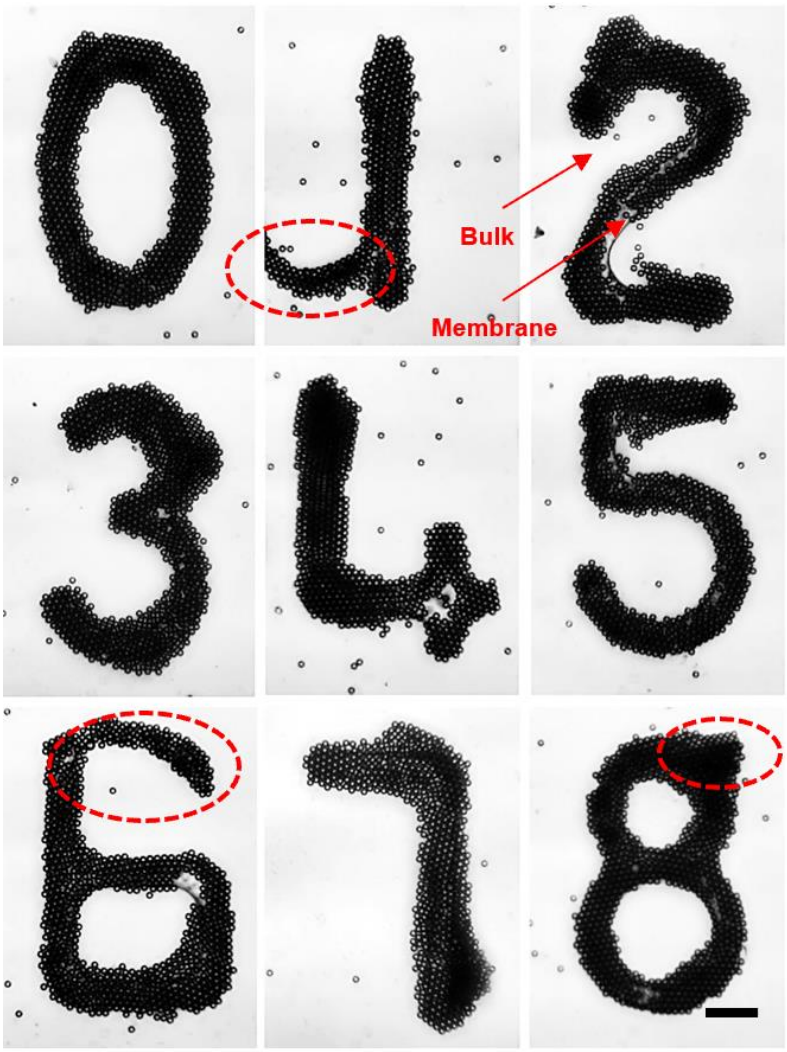

Figure 2.12 Patternings of micro-particles in water using soft, air-embedded PDMS structures in the shape of numeric characters. Soft PDMS enables precise and arbitrary patternings of 10 μm polystyrene beads. The traces, circled in red, occur due to waves' interferences. Scale bar, 70 μm.

channel shape for particle sorting. Overall, using the soft PDMS rather than the hard PDMS as the air-embedded structure leads to clean profiles of patternings.

To further assess CMAP's ability in complex and non-periodic patternings, we fabricated another set of soft, air-embedded PDMS structures consisted of numeric characters. At high concentration, **Figure 2.12** and **Video 4** in the supplementary materials, 10 μm polystyrene beads in water completely filled up the membrane regions, however, with additional traces circled in red that are especially noticeable in the

characters “1”, “6”, and “8”. This is due to the wave interferences between the neighboring air cavities when the size of bulk region exceeds the acoustic wavelength.

2.8 Device characterization through simplified finite element analysis (FEA) simulation

A simplified simulation approach accounting only the acoustics phenomenon may be used to characterize the CMAP device. The traces due to the wave interferences are well captured by the acoustic pressure simulation as shown in **Figure 2.13(a)** that considers only the pressure aspect among all the device phenomena incurred; the effect of fluid structure interaction was not accounted. The dark blue color represents the lowest value of absolute pressure mirroring the region of lowest acoustic potential. This is a simplified simulation technique compared to the acoustic-structural interaction simulation used previously, which involves multi-physics interactions that is far more complicated to simulate and requires much higher computing power.

To carry out the simplified approach, we also used Finite element (F.E.) solver COMSOL Multiphysics 5.3 as in the case for the acoustic-structural interaction. **Figure 2.13(b)** shows the 3-D model geometry implemented in the simulation; the geometry is constructed with true dimensions in accordance to the fabricated soft PDMS structures. Acoustic pressure module is implemented to simulate the pressure profile inside the device chamber. While the 3-D model geometry mimics the 2-D model in **Figure 2.3**, the bottom solid is treated as fluid rather than solid mechanics. This substitution eliminates the physics complication involved in the acoustic-structure interaction by considering only the materials’ impedance (given by speed of sound and density) to simulate the wave

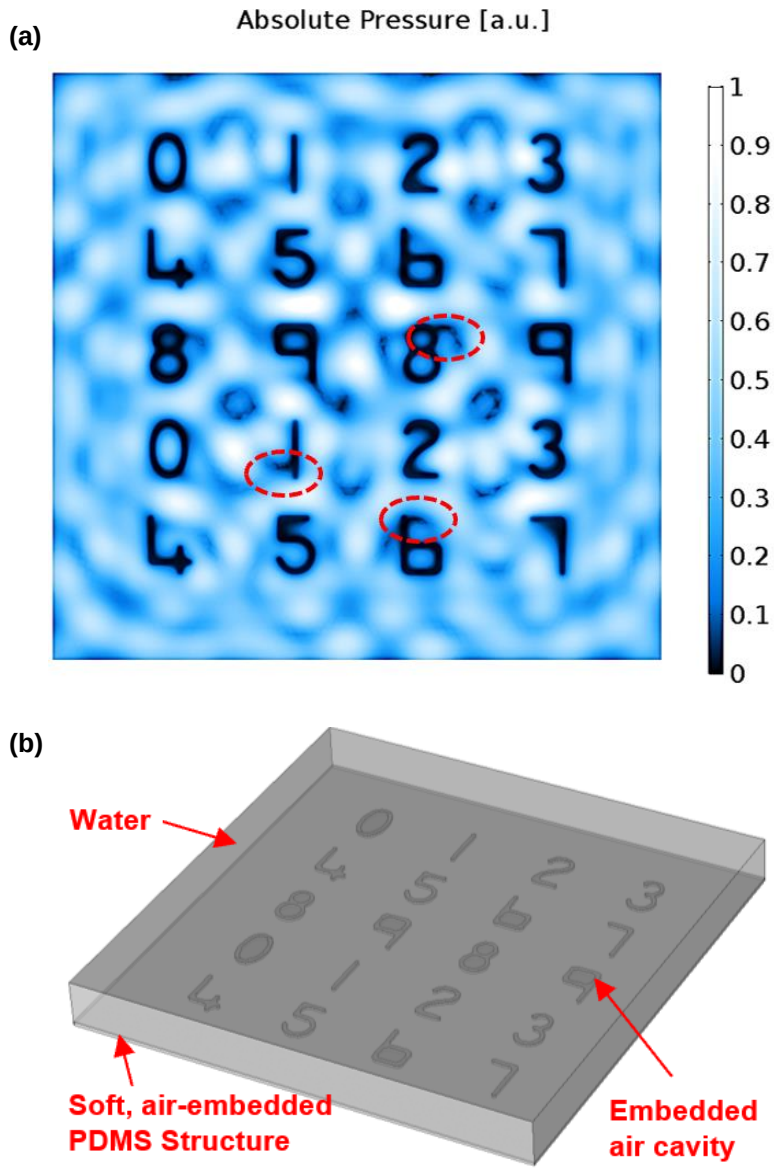

Figure 2.13 Corresponding acoustic pressure simulation of the patterned micro-particles in the shape of numeric characters. The simulated pressure landscape (**a**) that is directly above the PDMS structure follows closely to shape of the patterned profiles in **Figure 2.12**. Even the traces, circled in red, that occur due to waves' interferences resemble those in the patterned profiles. The simulation is performed using the 3-D model geometry (**b**), which consists of top fluid and bottom PDMS with embedded air cavities, similar as the acoustic-structure interaction model in **Figure 2.3**.

propagation. For the soft PDMS structure, arbitrary values of speed of sound and density are used. Normal displacement in the direction of y-axis is specified on the bottom of solid, simulating the direction of PZT excitation. Plane wave radiation is assumed all around the boundaries of the top fluid, enabling outgoing plane wave to leave the modeling domain

with minimal reflections. In short, the acoustic pressure simulation results show close resemblance with the experimental results which reflects the simplicity of using the CMAP mechanism to design/simulate a device that forms complex and non-periodic acoustic potential profiles.

2.9 Experimental demonstration of complex and non-periodic patternings of biological objects

Similar to polystyrene beads, patterning of cells highly depends on the surface displacement of the soft, air-embedded PDMS structure, as well as the density and compressibility of the particles and their surroundings, that gives rise to the acoustic potential landscape. HeLa cells are chosen here to testify the biocompatibility of the CMAP platform. For culturing, the cells (American Type Culture Collection, ATCC) were maintained in Dulbecco's modified essential medium (DMEM, Corning) supplemented with 10% (vol/vol) fetal bovine serum (FBS, Thermo Scientific), 1% penicillin/streptomycin (Mediatech), and 1% sodium pyruvate (Corning) and were kept in an incubator at 37°C and 5% CO2. Since typical cells ($\rho_p = 1068\, kg\, m^{-3}, \kappa_p = 3.77^{-10} Pa^{-1}$ as in the case of breast cells)[71] in DMEM have like properties as polystyrene beads in water, their potential landscapes formed using the same soft PDMS structure should be nearly identical. As illustrated in **Figure 2.14** and **Video 5** in the supplementary materials, patterning of HeLa cells in the shape of numeric characters resembles that of the polystyrene beads in **Figure 2.12**.

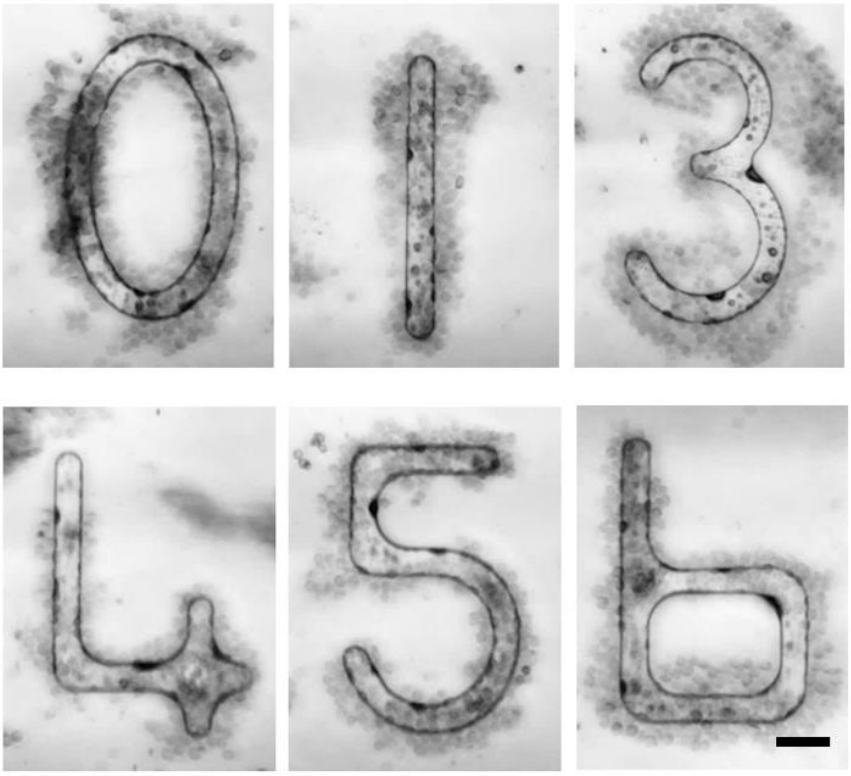

Figure 2.14 Patternings of HeLa cells in DMEM using soft, air-embedded PDMS structures in the shape of numeric characters. Similar to the polystyrene beads in **Figure 2.12**, HeLa cells can be patterned into arbitrary shapes using soft PDMS. Scale bar, 70 μm.

2.10 Viability assessment of the acoustic device platform

Numerous acoustic approaches for cell patterning have been assessed in determining the cell viability and proliferation, and prior approaches in the MHz-order acoustic fields have proven to be biocompatible[18], [47], [72], [73, p. 2]. Our CMAP device platform, in the similar MHz-order of operation, provides comparable results. To prevent potential thermal damage due to heat accumulation on our platform, we operated the device with a T.E. cooler set at 12 ºC to control the chamber temperature. **Figure 2.15(a)** illustrates the temperature as a function of time at the operating frequency of 3 MHz and voltage of 5 V_{rms}. The operation needs approximately 5 minutes before a steady state (~22 ºC) is reached, a temperature less than the cell incubation at 37 ºC.

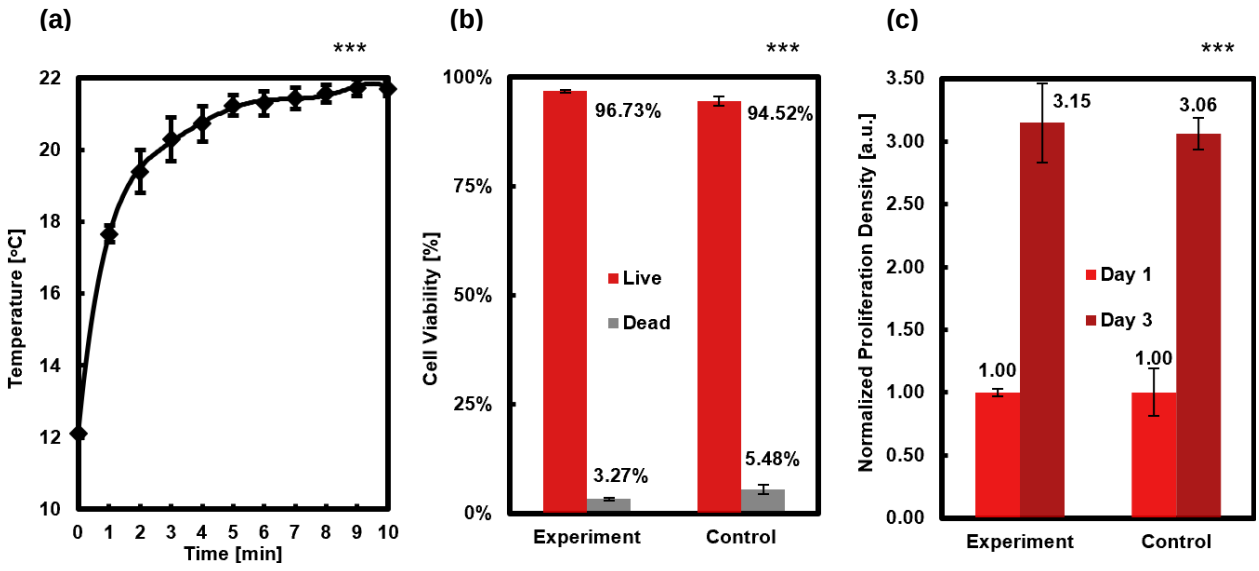

Figure 2.15 Viability assessments of HeLa cells in DMEM using soft, air-embedded PDMS structure. Due to heat generation of PZT, CMAP device platform is operated on a T.E. cooler to maintain the chamber temperature; the temperature as a function of time (**a**) is measured and the result shows a steady state at approximate 22 ºC. (**b**) After 5 min. of continuous operation in the device at the applied frequency of 3 MHz and voltage of 5 Vrms, cells show comparable viability at 96.73% to that of control at 94.52%. (**c**) Additionally, cells from both the control and experiment proliferated by more than three-folds over a two days period (48 hours), demonstrating the biocompatibility of the CMAP platform. Scale bar, 70 µm. (***Number of trials measured, n = 3)

Furthermore, viability assessment using Trypan blue (ATCC) and cell counts using hemacytometer (Hausser Scientific Reichert Bright-Line), following the manufacturers' protocols, are performed on the HeLa cells operated in the device under the same experimental condition for 5 minutes; outcome shows similar level of viability at 96.73% as compared to that of control at 94.52%, **Figure 2.15(b)**. Assessment on the cell proliferation also shows promising results. After the experiment, portion of the cells were incubated for 48 hours (from Day 1 to Day 3). Using hemocytometer, we have approximated the densities of cells at Day 1 and at Day 3 for both the experiment and control which all indicate an increase by more than three folds, **Figure 2.15(c)**. The increase corresponds to the HeLa cell doubling time that is approximately 24 hours[74].

2.11 Discussion

We have demonstrated the CMAP platform as a powerful tool to realize deep sub-wavelength, complex and non-periodic patternings of microparticles and biological objects. These are achieved using a suspended, thin and compliant PDMS membrane that minimizes the effect of structure-induced vibration and that adapts to the surrounding fluid motion without offsetting the intended acoustic potential landscape. The membrane can be of any geometry, making complex and non-periodic patternings possible. Additionally, both the PZT and the soft, air-embedded PDMS structure can be scaled up for larger area patterning based on the underlying acoustic actuation principle.

Of note here is that since the ARF in **Equation 2(b)** includes both the velocity and pressure terms which usually coupled in practical applications, it is difficult to design a device optimized for acoustic patterning that utilizes both terms. For the CMAP platform, the device is designed for the patterning based on the pressure term. Microparticles, such as the polystyrene beads and most biological objects, that have a similar density but different compressibility from water ($f_1 \gg f_2$) are ideal objects to be patterned on the CMAP device. For particles with large density difference from water such as gold beads ($f_1 \sim 0.99$, $f_2 \sim 0.90$), the velocity term can become significant. Nevertheless, the patterns formed by these particles should also conform to the shape of air cavities since the cavity edges are where maximum velocity locates as shown in **Figure 2.5(b)**.

Although acoustic streaming force, ASF[51], can be induced to counterbalance the ARF and disturb the patterning, our experimental results suggest that ARF is the driving force when the operation frequency is above 3 MHz and the particle is sized 10 μm or larger. At the onset of the operation, streaming vortices, as illustrated by the 1 μm

polystyrene beads (fluorescent green polystyrene beads from Thermo Fisher Scientific) in **Video 3** in the supplementary materials, are observed only at the center of the circular membrane and extend weakly to ~25 μm near the edge. On the other hand, the 10 μm polystyrene beads that were spread across the device migrate toward the membrane edges, where they are trapped firmly despite the later bulk movement of fluid as shown by the 1 μm beads. This strong trapping effect implies dominant strength of ARF to the patterning of 10 μm beads. We also refer the observed phenomenon of the bulk movement as global flow, induced from the volumetric change of chamber as the upper PDMS lid expands thermally due to the heat generation from PZT. Since the upper PDMS lid (~1 cm) is substantially thicker than the bottom soft, air-embedded PDMS structure (~27 μm), the volumetric change should be predominately caused by the expansion of the lid.

PDMS is a material with strong acoustic energy attenuation property, a potential problem that needs to be properly addressed when designing acoustofluidics devices. In our CMAP device, the acoustic waves generated at the bottom substrate propagate through the thin, air-embedded PDMS structure, into the chamber fluid, and then into the PDMS lid. The thickness of the lid is designed to be 1 cm, which enables sufficient wave energy attenuation at our operating frequency of 3 MHz to prevent reflection from the interface between the ambient air and device. At 3 MHz, the attenuation coefficient of PDMS is 10.14 dB/cm, which allow the lid to absorb >99% of wave energy before reflecting back to the chamber fluid[64], [65]. Note that the thickness of the air-embedded PDMS structure at 27 μm is much smaller than that of the lid, rendering the wave energy attenuation at the structure to be negligible.

Video 4 and 5 in the supplementary materials show that the 10 μm polystyrene beads and HeLa cells, respectively, outside the air cavities get drifted away because these are the excessive targets as to what the potential wells above the cavities can hold. Note that such drifts are mainly caused by the global flow for the reason that the ASF is only effective nearby the membrane edges. The drifts are favorable to us because they lead to overall cleaner patterning profiles without excessive targets outside the cavities. Notice that the images in **Video 3, 4, and 5** get blurred toward the end. We suspect that the thermal expansion of PDMS has caused structural deformation which affected the microscope focusing. Besides the global flow, patternings of the 10 μm beads and HeLa cells reveal conformities to the pressure distribution simulated in **Figure 2.13(a)**, further defying the significance of acoustic streaming.

We have chosen 3 MHz as the operation frequency because it is a high enough value to suppress the acoustic streaming flow and a low enough value to avoid extra acoustic heating. For example, when the operation frequency is lowered to 0.5 MHz, 10 μm polystyrene beads can follow the streamlines of 1 μm beads, circulating in vortex form near the membrane edges as demonstrated by **Video 6** in the supplementary materials. This leads to unstable patterning and difficulty in achieving desired profile. On the other hand, while operation at higher frequency can minimize the streaming flow, it is accompanied by larger energy attenuation in PDMS and, thus, extra heat generation that needs to be managed[64].

While the CMAP platform relies on compliant, viscoelastic PDMS membrane to provide the breakthroughs in patterning, the membrane is so thin (~2 μm) that the above fluid can penetrate through. This is evident by the fluid droplets below the membrane

regions as shown in **Figure 2.10**. Prior literatures[75], [76] , too, have demonstrated that PDMS is porous in nature which enables water molecules to diffuse through. Accounting for the additional acoustic vibrations during the device operation, the fluid could have penetrated through the thin membrane which generated the droplets. Accumulation of the droplets could also affect particle patterning; if sufficient droplets are accumulated (e.g. filling up the air cavities), the membrane would no longer be fluid compliant and the patterning profile would be distorted. Nevertheless, the patterning process of the CMAP platforms takes less than 20 seconds to complete, substantially less than the time it takes for droplets to fill the cavities as observed experimentally.

Chapter 3

Field-Programmable Acoustic Array for Patterning Micro-objects

3.1 Introduction

Recent advancements in acoustics have led to the increase in Degree-of-Freedom (DOF) of manipulating biological objects. Starting with single-cell patterning, acoustics has evolved such that the size of acoustic potential well can be optimized to allow only a single cell to occupy. The impact is profound for many biomedical applications[1], [7], [8], [77], [78], especially for large batch single-cell analysis[6]. Furthermore, three-dimensional phase-shifting based acoustic manipulation technology allows picking up and releasing single cells one by one[20]. In order to generate non-uniform potential fields however, BAWs and SAWs devices typically rely on forming acoustic standing waves created by resonant cavities and interdigitated transducers (IDTs), respectively. For BAWs, one drawback is that the potential profile is predetermined by the structural design of the devices, which fundamentally prevents the patterning profile to be versatile and re-configurable. For SAWs devices, although the potential profile can be adjusted by changing the phases and frequencies of the electrical signals applied to the IDTs[18], [79], [80], complex patterning profiles are only obtained for single-particle manipulation whereas the profiles for multi-particles manipulation are simple and periodic. Additionally,

the introduced CMAP platform depends on the predefined, air-embedded PDMS structure to shape the profile of acoustic wells. Creating a new profile would require a different physical PDMS structure to be fabricated. As results, these acoustofluidic methods are limited to provide high-resolution and re-configurable potential profiles without having a new device design.

3.2 Device design and operation principle

In this chapter, we present a Field-Programmable Acoustic Array (FPAA) in which the acoustic potential profile can be optically re-configured for patterning micro-particles into complex shape with sub-wavelength resolution. Similar as the CMAP, FPAA platform, **Figure 3.1**, uses a combined PZT and a 1 μm thick hydrogenated amorphous silicon (a-Si:H) film coated glass substrate to house the soft, air-embedded PDMS structure that is molded into an array of squared air cavities. The experimental procedures can be explained in 4 steps. Initially, Dulbecco's modified essential medium (DMEM) from Corning is dispensed over the surface of the fabricated PDMS structure, **Figure 3.1(a)**. Through a vacuuming process, the fluid sips through the porous PDMS membrane[75], [76], converting the air-embedded structure into fluid-embedded structure **Figure 3.1(b)**. DMEM, containing mostly water, is used for its similar acoustic impedance to that of PDMS[55]. We have also experimentally observed that DMEM sips through the PDMS membrane easier than does DI water, possibly due to surface tension related properties. Any excessive DMEM on the PDMS surface is removed thereafter. Next, by focusing a continuous wave (CW) laser of 532 nm wavelength onto the a-Si:H layer, the fluid within a selected cavity is heated and vaporized, **Figure 3.1(c)**. As results, a series of cavities

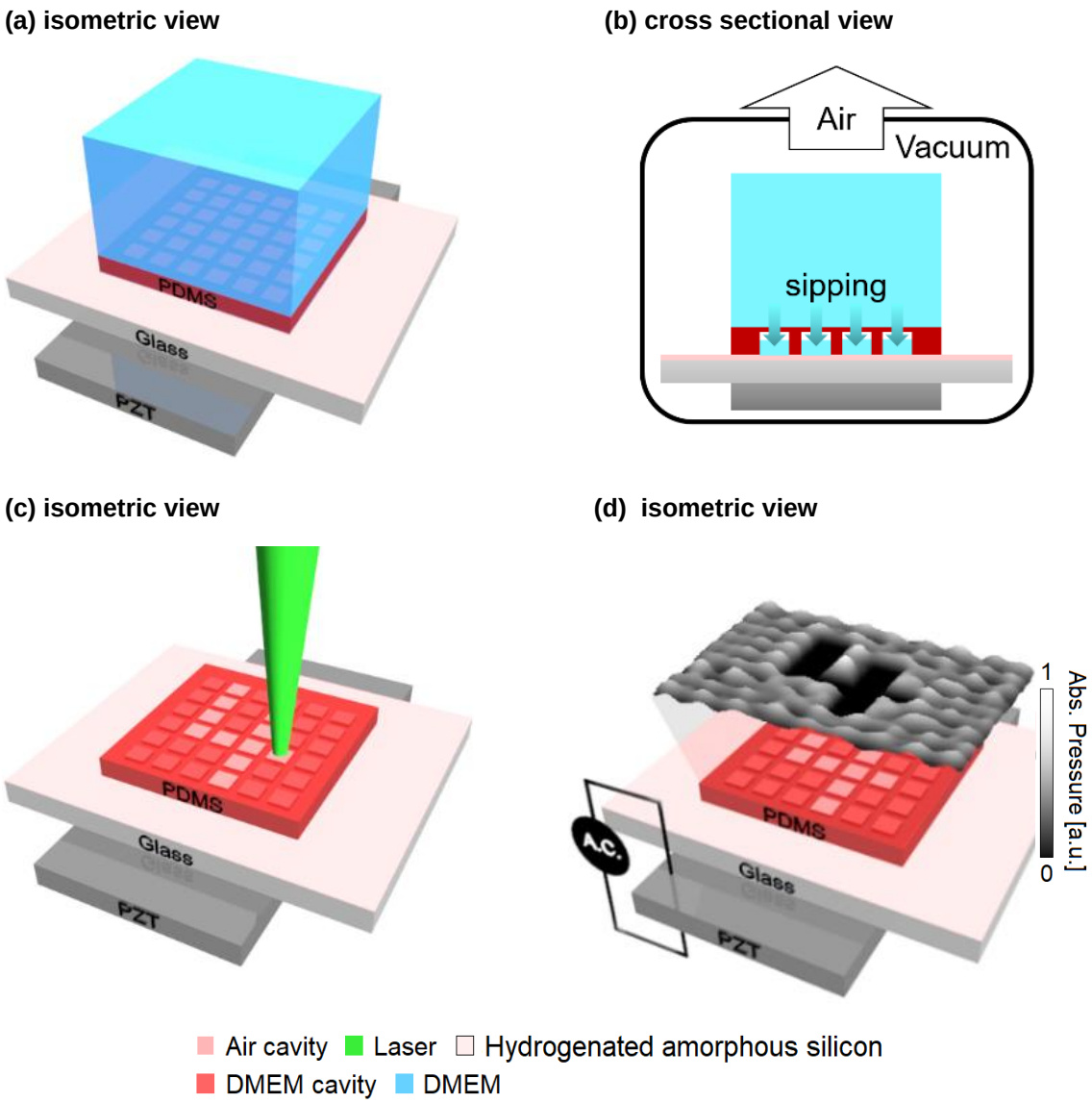

Figure 3.1 Device schematics illustrating the operation of field-programmable acoustic platform. The operation consists of 4 steps. Firstly, DMEM is dispensed over the PDMS structure (**a**). Secondly, vacuuming is performed to fill the air cavities with the fluid by sipping through the PDMS membrane (**b**). Thirdly, a focused laser beam is scanned through the fluid-embedded structure to selectively revert the fluid cavities to air cavities (**c**). Lastly, PZT is activated which enables acoustic waves to pass through the transformed structure to form the patterned, acoustic potential profile (**d**).

can be converted by scanning the laser beam across the PDMS structure, forming a desired shape like the numeric letter “4”. The vapor created can diffuse through the PDMS membrane into the above air ambience. Subsequent activation of the PZT generates an acoustic potential profile based on the laser-created air cavities pattern, **Figure 3.1(d)**. If

a fluid sample containing micro-particles is dispensed over the transformed structure, the particles will align in respect to the patterned potential profiles. Essentially, scanning the laser through the fluid cavities turns them into air cavities, which will act as a single combined cavity. Reprogramming the platform can be done by reapplying the vacuuming step introduced in **Figure 3.1(b)**, which refills all cavities with fluid.

3.3 Device characterization through finite element analysis (FEA) simulation

Spacing among these air cavities is a crucial parameter. Too large a spacing prevents the acoustic potential profiles of neighboring air cavities from merging into one. To investigate such effect, we simulated the acoustic-structure interaction using a finite element model (COMSOL Multiphysics 5.3) and followed the simulation technique introduced for the CMAP platform. An array of 30 μm wide air cavities is simulated with varying spacings under a sinusoid excitation frequency of 3 MHz. The 30 μm cavity width is chosen to ensure sufficient attenuation of waves propagating into the PDMS membrane in order to avoid distortion to the potential profile generated. Based on the CMAP's simulation, the attenuation length from the bulk into the membrane is estimated to be 10 μm for a 2 μm thick soft PDMS. The results, **Figure 3.2**, show noticeable differences in the normalized acoustic radiation potential profiles, calculated based on 10 μm polystyrene beads in DI water, for cavity spacing between 60 μm and 10 μm. The potential profile for the 60 μm spacing case, **Figure 3.2(a)**, fluctuates with energy dips at the edges of air cavities, where the beads will tend to accumulate in the early stage of patterning. Such characteristic is attributed to the dominance of the velocity term in **Equation 2(b)** due to the large membrane vibration near the membrane edges. For the 10 μm spacing

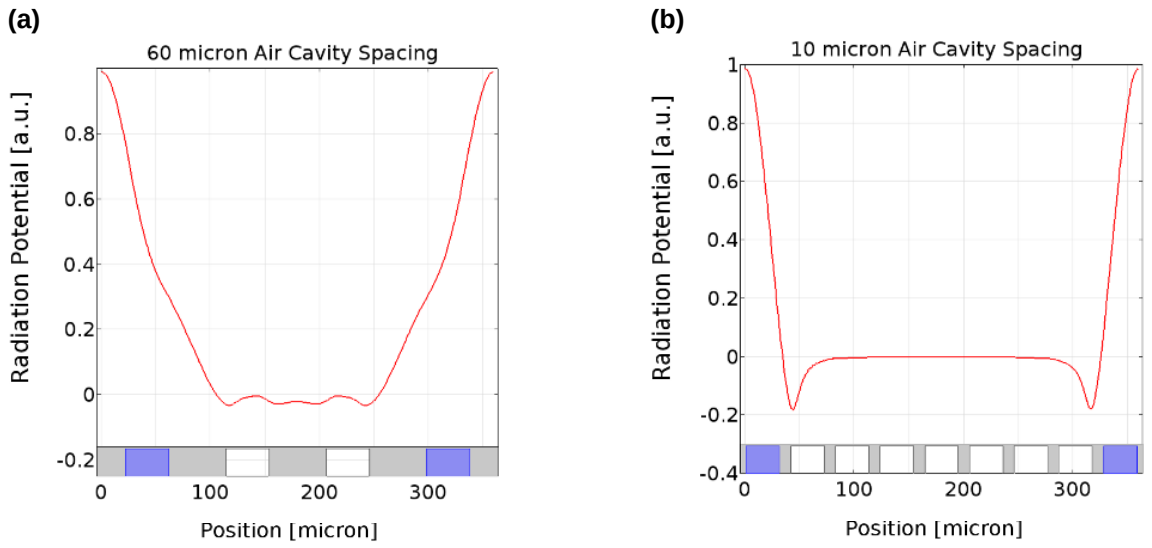

Figure 3.2 Simulated, normalized acoustic potential profiles for an array of air cavities of 30 μm in width with varying cavity spacings. At 60 μm spacing **(a)**, the profile that is 5 μm above the cavities fluctuates with dips at the cavity edges. At 10 μm spacing **(b)**, the profile becomes nearly flat across the cavities with dips only at the edges of the outer most cavities. Cavities in white represent air and cavities in blue represent fluid.

case, **Figure 3.2(b)**, the potential profile is smooth and flat with the dips only at the outer most air cavities. This effect allows the potential profiles created by discrete air cavities to be merged into one profile of desired shape.

To verify this coalescent effect, we also examined the impact of changing the number of nearby air cavities. Results, **Figure 3.3**, show that the coalescent effect holds, and varying the number of cavities essentially changes the size of the merged acoustic potential well. Under this 10 μm spacing design therefore, re-configurable patterning can be achieved. Notice at our operating frequency of 3 MHz, the wavelength in water is ~500 μm, which is substantially larger than the cavities' width and spacing. This demonstrates that the FPAA allows the formation of acoustic potential profile with sub-wavelength resolution.

3.4 Device setup and operation

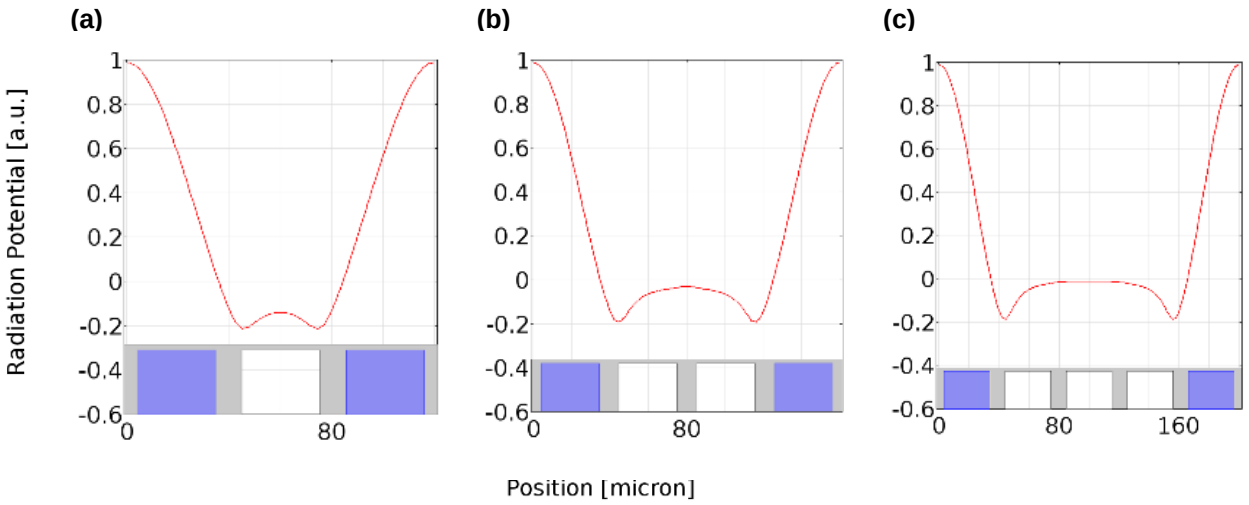

Figure 3.3 Simulated, normalized acoustic potential profiles for an array of varying number of air cavity with a width of 30 μm and fixed spacing of 10 μm. The results for a single air cavity **(a)**, two air cavities **(b)**, and three air cavities **(c)** show similar profile shapes that have the lowest energy dips at the edges of the outer most cavities. Cavities in white represent air and cavities in blue represent fluid.

To verify the simulation results, we carried out experiments following the setup shown in **Figure 3.4**. Similar as the CMAP platform, FPAA platform operates on a T.E. cooler set at 12°C to prevent overheating of the fluid sample due to heat generation from the PZT; at the operating parameters of 3 MHz and 5 V_{rms}, the fluid sample can be maintained at 23°C. The platform is electrically connected to a power amplifier (ENI Model 2100L) and a function generator (Agilent Model 33220A) for the PZT excitation. To generate a focused laser beam onto the platform, we used a CW diode pumped, solid state green laser (CrystaLaser CL532-300-O) of 532 nm wavelength and re-adjusted the laser spot size through a lens tube. Inside the tube, 3 lenses with Effective Focal Lengths of 25 mm, 200 mm, and 125 mm are positioned to produce a laser spot size of ~23 μm on the platform. A 50/50 beamsplitter cube is integrated to redirect the laser beam as shown. With a 1 μm thick a-Si:H layer on the platform, a laser power of ~17 mW is sufficient to induce vaporization of DMEM medium within a squared cavity sized at 30 μm X 30 μm X 25 μm in approximately 1 sec as observed experimentally (See **Video 7** in the

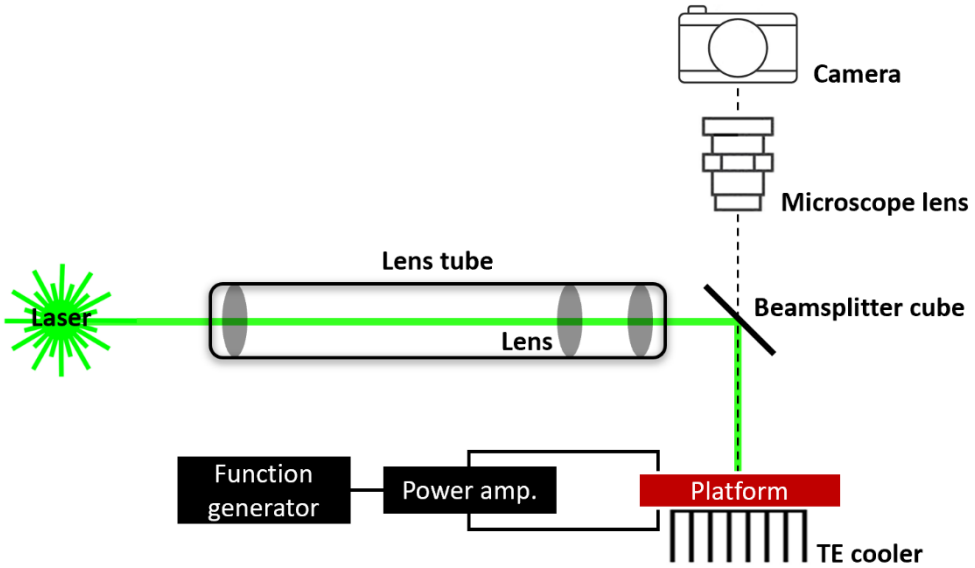

Figure 3.4 Experimental setup of the field-programmable platform

supplementary materials for the laser vaporization process). To view and record the patterning process, we used an ultra-long working distance microscope lens (20× Mitutoyo Plan Apo) along with a camera (Zeiss Model AxioCam mRm) mounted on an upright microscope (Zeiss Model Axioskop 2 FS).

3.5 Experimental demonstration of complex and non-periodic patternings of micro-particles

Using the experimental setup and FPAA platform, a sample of 10 µm polystyrene beads in DMEM is dispensed over a patterned PDMS structure. The results of the beads' profiles obtained match those of the simulations. **Figure 3.5(a) – (c)** experimentally illustrate the coalescent effect of squared air cavities of width 30 µm spaced 10 µm apart. In **Figure 3.5(a)**, beads are distributed around the edges of a single air cavity where the lowest acoustic potential resides. With two and three air cavities, **Figure 3.5(b) and (c)**, beads are distributed only at the outer most edges of the cavities. In between the cavities,

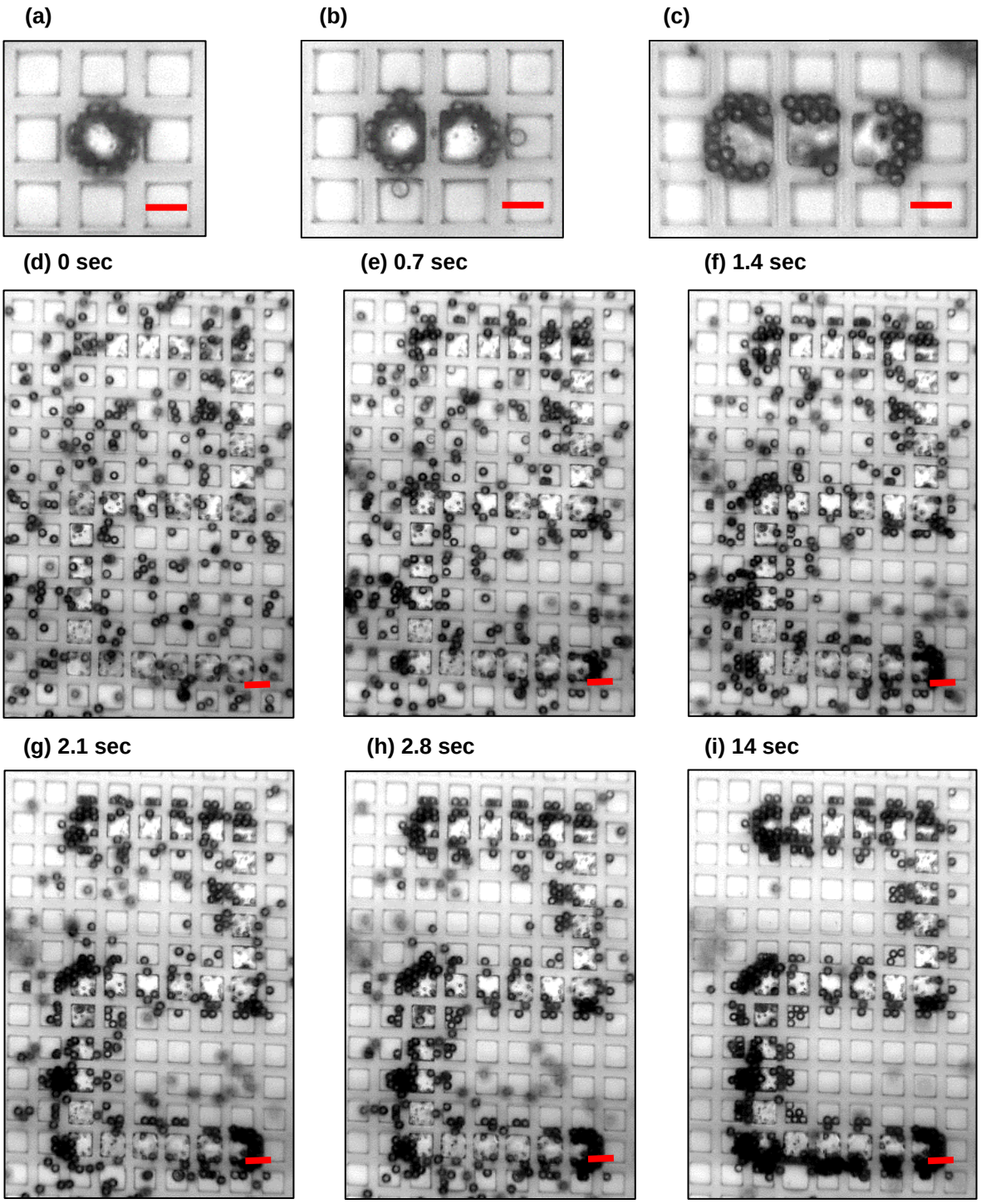

Figure 3.5 Experimental demonstrations for conforming the simulation results through patterning of 10 μm polystyrene beads. Experimental results for a single air cavity **(a)**, two air cavities **(b)**, and three air cavities **(c)** conform to the simulation results in **Figure 3.3**. Shown in **(d) – (i)** is a patterning process for numeric letter “2”. Scale bar, 30 μm.

beads do not occupy; such phenomenon confirms the coalescent effect of potential

profiles created by closely spaced air cavities.

To demonstrate the patterning capability of the FPAA platform, we patterned micro-particles into complex and non-periodic shapes. Shown in **Figure 3.5(d) – (i)** are snapshots of the process for 10 μm polystyrene beads to form into a letter “2”. In **Figure 3.5(i)**, majority of the micro-particles trapped along the outer most edges of air cavities matches with what is predicted by the simulation. See **Video 8** in the supplementary materials for the complete patterning process. More patterning examples are demonstrated in **Figure 3.6**. Beads’ patterning profiles before and after are shown in the shape of numeric letters “0”, “1”, “5”, “6”, “7”, and “8”. In lower concentration, beads’ accumulation follows the contour of air cavities at the outer edges. In higher concentration, beads’ accumulation covers the entire surface of air cavities. Such difference between lower and higher concentrations can be observed even within the same patterning profile. Additionally, the profiles can be affected by the wave interferences from nearby air cavities.

3.6 Discussion

A field-programmable acoustic array (FPAA) has been demonstrated. Such platform is capable of re-configurable patterning of micro-objects into complex and non-periodic shapes at 40 μm resolution under the excitation of 3MHz signals. Higher resolution is possible through increasing the acoustic frequencies, yet, effects such as increased energy absorption may need to be properly managed. In FPAA, programmable patterning is realized by applying laser heating to selectively vaporize fluid in a two-dimensional PDMS micro-cavities array. With the spacing between cavities reduced to 10

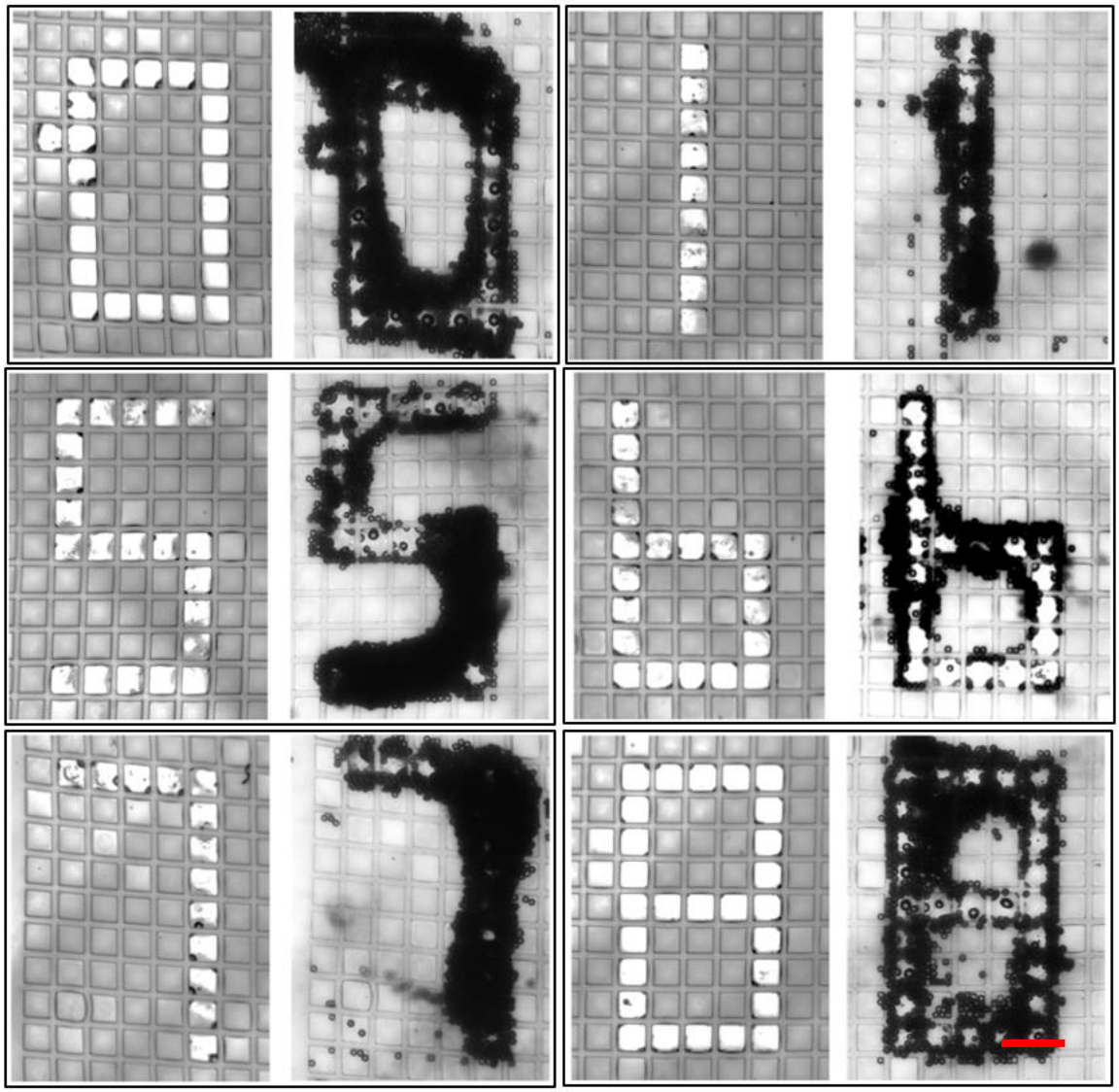

Figure 3.6 Examples of complex patterning of 10 µm polystyrene beads into various numeric letter shapes "0", "1", "5", "6", "7", and "8". Scale bar, 80 µm.

µm, acoustic potential profiles generated by neighboring cavities can be merged to form an integrated complex potential profile. Reprogramming is realized by simply reapplying a vacuuming step to refill the air cavities with fluid that resets the platform. With the described features, FPAA is versatile for the applications in microfluidics such as biological micro-particle patterning, sorting, tissue engineering, and advanced manufacturing for 3D printing.

Chapter 4

Conclusion

Manipulation of biological objects is essential in facilitating applications, such as single-cell analysis, cell-cell interactions, tissue engineering, drug delivery, etc. in the biomedical discipline. In order to achieve the manipulation, several physical mechanisms have been devised to be integrated into LOC devices. Conventional mechanisms include DEP, magnetic, optical, and acoustic mechanisms, and each of them has advantages and disadvantages over one another. In comparison, acoustofluidics have been demonstrated to have superior biocompatibility and wide window of operable object sizes.

Acoustic mechanism can generally be categorized into two approaches: BAWs and SAWs approaches. Both approaches utilize standing waves method to generate the non-uniform field needed to induce the acoustic radiation force for manipulation of objects. However, this method poses fundamental limitations. While BAWs approach has the potential to create complex patterning profiles of particles, it has limited resolution that is half the wavelength; for practical applications, BAWs devices operate in the low-MHz regime which translates to a few hundreds of micron of resolution in water, substantially larger than a typical cell size. While SAWs devices operating in much higher-MHz regime produce resolution in the same order of magnitude as cell size, they are limited to create

complex profiles due to the confined orientation of waves generation of the $LiNbO_3$ substrate.

In order to overcome the limitations, CMAP platform is devised. Rather than relying on standing waves to create acoustic potential wells, CMAP platform utilizes deep, sub-wavelength method to control the incoming travelling wave fronts with resolution less than half the wavelength. Through the integration of a fluid compliant membrane encapsulating air cavities embedded within a soft PDMS structure, the platform minimizes the coupled fluid-structure vibration between the fluid medium and membrane which enables shape-creation of acoustic wells conforming to that of air cavities. Since the cavities can be fabricated into complex shapes and sizes, the acoustic wells generated can also be complex. With such device design, we have succeeded in high-resolution, complex patterning profiles of micro-particles and HeLa cells as demonstrated by our experiments that achieved one tenth of the wavelength resolution, 5 times enhancement over the conventional BAWs and SAWs devices. Patterning area of 3 X 3 mm^2 has also been demonstrated with the potential to be sized up further.

By incorporating a photothermal mechanism into the CMAP platform, we have devised the FPAA platform that enables re-configurable patterning of micro-objects into high-resolution, complex profiles. Not only the FPAA platform allows real-time, versatile adjustment to the shape of acoustic potential well but also allows the platform to be repeatedly used, achieving the functionality of re-configuring potential profile that no other acoustic device has succeeded in.

In summary, our CMAP platform has opened a new scientific frontier using the deep, sub-wavelength patterning method in contrary to the standing waves method used

by traditional acoustic devices. In addition to the advantages introduced by the CMAP platform, the FPAA platform have furthered the capability in manipulating micro-objects by enabling the induced acoustic potential profile to become re-configurable. As implied, the technological advancements to the applications, such as biological objects' patterning, sorting, tissue engineering, etc., that the CMAP and FPAA platforms can bring to the biomedical discipline is immense.

Reference

[1] J. Nilsson, M. Evander, B. Hammarström, and T. Laurell, “Review of cell and particle trapping in microfluidic systems,” *Analytica Chimica Acta*, vol. 649, no. 2, pp. 141–157, Sep. 2009, doi: 10.1016/j.aca.2009.07.017.

[2] J. Sun, N. Jamilpour, F.-Y. Wang, and P. K. Wong, “Geometric control of capillary architecture via cell-matrix mechanical interactions,” *Biomaterials*, vol. 35, no. 10, pp. 3273–3280, Mar. 2014, doi: 10.1016/j.biomaterials.2013.12.101.

[3] J. Sinclair *et al.*, “A Cell-Based Bar Code Reader for High-Throughput Screening of Ion Channel−Ligand Interactions,” *Anal. Chem.*, vol. 74, no. 24, pp. 6133–6138, Dec. 2002, doi: 10.1021/ac026133f.

[4] J. Liu *et al.*, “Functional three-dimensional HepG2 aggregate cultures generated from an ultrasound trap: Comparison with HepG2 spheroids,” *J. Cell. Biochem.*, vol. 102, no. 5, pp. 1180–1189, Dec. 2007, doi: 10.1002/jcb.21345.

[5] D. K. Wood, D. M. Weingeist, S. N. Bhatia, and B. P. Engelward, “Single cell trapping and DNA damage analysis using microwell arrays,” *Proceedings of the National Academy of Sciences*, vol. 107, no. 22, pp. 10008–10013, Jun. 2010, doi: 10.1073/pnas.1004056107.

[6] D. J. Collins, B. Morahan, J. Garcia-Bustos, C. Doerig, M. Plebanski, and A. Neild, “Two-dimensional single-cell patterning with one cell per well driven by surface acoustic waves,” *Nature Communications*, vol. 6, p. 8686, Nov. 2015, doi: 10.1038/ncomms9686.

[7] L. Kang, “Microfluidics for drug discovery and development: From target selection to product lifecycle management,” *Drug Discovery Today*, vol. 13, no. 1–2, pp. 1–13, Jan. 2008, doi: 10.1016/j.drudis.2007.10.003.

[8] C. M. Puleo, H.-C. Yeh, and T.-H. Wang, “Applications of MEMS Technologies in Tissue Engineering,” *Tissue Engineering*, vol. 13, no. 12, pp. 2839–2854, Dec. 2007, doi: 10.1089/ten.2007.0214.

[9] N. Jamilpour, K.-H. Nam, C. C. Gregorio, and P. K. Wong, “Probing Collective Mechanoadaptation in Cardiomyocyte Development by Plasma Lithography Patterned Elastomeric Substrates,” *ACS Biomater. Sci. Eng.*, Dec. 2018, doi: 10.1021/acsbiomaterials.8b00815.

[10] “Ageing | United Nations.” [Online]. Available: https://www.un.org/en/sections/issues-depth/ageing/. [Accessed: 20-Jan-2020].

[11] C.-T. Ho *et al.*, “Liver-cell patterning Lab Chip: mimicking the morphology of liver lobule tissue,” *Lab on a Chip*, vol. 13, no. 18, pp. 3578–3587, 2013, doi: 10.1039/C3LC50402F.

[12] M.-Y. Chiang, Y.-W. Hsu, H.-Y. Hsieh, S.-Y. Chen, and S.-K. Fan, “Constructing 3D heterogeneous hydrogels from electrically manipulated prepolymer droplets and crosslinked microgels,” *Science Advances*, vol. 2, no. 10, p. e1600964, Oct. 2016, doi: 10.1126/sciadv.1600964.

[13] I.-F. Cheng, H.-C. Chang, D. Hou, and H.-C. Chang, “An integrated dielectrophoretic chip for continuous bioparticle filtering, focusing, sorting, trapping,

and detecting," *Biomicrofluidics*, vol. 1, no. 2, p. 021503, May 2007, doi: 10.1063/1.2723669.
[14] B. Raeymaekers, C. Pantea, and D. N. Sinha, "Manipulation of diamond nanoparticles using bulk acoustic waves," *Journal of Applied Physics*, vol. 109, no. 1, p. 014317, Jan. 2011, doi: 10.1063/1.3530670.
[15] I. Leibacher, P. Reichert, and J. Dual, "Microfluidic droplet handling by bulk acoustic wave (BAW) acoustophoresis," *Lab on a Chip*, vol. 15, no. 13, pp. 2896–2905, 2015, doi: 10.1039/C5LC00083A.
[16] B. Hammarström, T. Laurell, and J. Nilsson, "Seed particle-enabled acoustic trapping of bacteria and nanoparticles in continuous flow systems," *Lab on a Chip*, vol. 12, no. 21, pp. 4296–4304, 2012, doi: 10.1039/C2LC40697G.
[17] A. Castro and M. Hoyos, "Study of the onset of the acoustic streaming in parallel plate resonators with pulse ultrasound," *Ultrasonics*, vol. 66, pp. 166–171, Mar. 2016, doi: 10.1016/j.ultras.2015.10.019.
[18] X. Ding *et al.*, "On-chip manipulation of single microparticles, cells, and organisms using surface acoustic waves," *Proceedings of the National Academy of Sciences*, vol. 109, no. 28, pp. 11105–11109, Jul. 2012, doi: 10.1073/pnas.1209288109.
[19] X. Ding, J. Shi, S.-C. Steven Lin, S. Yazdi, B. Kiraly, and T. Jun Huang, "Tunable patterning of microparticles and cells using standing surface acoustic waves," *Lab on a Chip*, vol. 12, no. 14, pp. 2491–2497, 2012, doi: 10.1039/C2LC21021E.
[20] F. Guo *et al.*, "Three-dimensional manipulation of single cells using surface acoustic waves," *PNAS*, vol. 113, no. 6, pp. 1522–1527, Feb. 2016, doi: 10.1073/pnas.1524813113.
[21] A. K. Tay, M. Dhar, I. Pushkarsky, and D. D. Carlo, "Research highlights: manipulating cells inside and out," *Lab on a Chip*, vol. 15, no. 12, pp. 2533–2537, 2015, doi: 10.1039/C5LC90060C.
[22] G. Destgeer and H. Jin Sung, "Recent advances in microfluidic actuation and micro-object manipulation via surface acoustic waves," *Lab on a Chip*, vol. 15, no. 13, pp. 2722–2738, 2015, doi: 10.1039/C5LC00265F.
[23] S.-C. Steven Lin, X. Mao, and T. Jun Huang, "Surface acoustic wave (SAW) acoustophoresis: now and beyond," *Lab on a Chip*, vol. 12, no. 16, pp. 2766–2770, 2012, doi: 10.1039/C2LC90076A.
[24] Y. Chen *et al.*, "Tunable Nanowire Patterning Using Standing Surface Acoustic Waves," 09-Apr-2013. [Online]. Available: https://pubs.acs.org/doi/abs/10.1021/nn4000034. [Accessed: 01-Apr-2019].
[25] Y. Bian *et al.*, "Acoustofluidic waveguides for localized control of acoustic wavefront in microfluidics," *Microfluid Nanofluid*, vol. 21, no. 8, p. 132, Jul. 2017, doi: 10.1007/s10404-017-1971-y.
[26] A. R. Rezk, J. K. Tan, and L. Y. Yeo, "HYbriD Resonant Acoustics (HYDRA)," *Advanced Materials*, vol. 28, no. 10, pp. 1970–1975, 2016, doi: 10.1002/adma.201504861.
[27] B. Kang *et al.*, "High-resolution acoustophoretic 3D cell patterning to construct functional collateral cylindroids for ischemia therapy," *Nature Communications*, vol. 9, no. 1, Dec. 2018, doi: 10.1038/s41467-018-07823-5.

[28] W. Connacher *et al.*, “Micro/nano acoustofluidics: materials, phenomena, design, devices, and applications,” *Lab Chip*, vol. 18, no. 14, pp. 1952–1996, Jul. 2018, doi: 10.1039/C8LC00112J.
[29] M. Alvarez, J. R. Friend, and L. Y. Yeo, “Surface Vibration Induced Spatial Ordering of Periodic Polymer Patterns on a Substrate,” *Langmuir*, vol. 24, no. 19, pp. 10629–10632, Oct. 2008, doi: 10.1021/la802255b.
[30] W. Hu, Q. Fan, and A. T. Ohta, “An opto-thermocapillary cell micromanipulator,” *Lab on a Chip*, vol. 13, no. 12, pp. 2285–2291, 2013, doi: 10.1039/C3LC50389E.
[31] M.-C. Zhong, X.-B. Wei, J.-H. Zhou, Z.-Q. Wang, and Y.-M. Li, “Trapping red blood cells in living animals using optical tweezers,” *Nature Communications*, vol. 4, p. 1768, Apr. 2013, doi: 10.1038/ncomms2786.
[32] A. Ashkin, J. M. Dziedzic, and T. Yamane, “Optical trapping and manipulation of single cells using infrared laser beams,” *Nature*, vol. 330, no. 6150, pp. 769–771, Dec. 1987, doi: 10.1038/330769a0.
[33] H. Zhang and K.-K. Liu, “Optical tweezers for single cells,” *Journal of The Royal Society Interface*, vol. 5, no. 24, pp. 671–690, Jul. 2008, doi: 10.1098/rsif.2008.0052.
[34] D. Di Carlo, L. Y. Wu, and L. P. Lee, “Dynamic single cell culture array,” *Lab on a Chip*, vol. 6, no. 11, pp. 1445–1449, 2006, doi: 10.1039/B605937F.
[35] L. Lin, Y.-S. Chu, J. Paul Thiery, C. Teck Lim, and I. Rodriguez, “Microfluidic cell trap array for controlled positioning of single cells on adhesive micropatterns,” *Lab on a Chip*, vol. 13, no. 4, pp. 714–721, 2013, doi: 10.1039/C2LC41070B.
[36] M. Chanasakulniyom, A. Glidle, and J. M. Cooper, “Cell proliferation and migration inside single cell arrays,” *Lab on a Chip*, vol. 15, no. 1, pp. 208–215, 2015, doi: 10.1039/C4LC00774C.
[37] A. M. Skelley, O. Kirak, H. Suh, R. Jaenisch, and J. Voldman, “Microfluidic Control of Cell Pairing and Fusion,” *Nat Methods*, vol. 6, no. 2, pp. 147–152, Feb. 2009, doi: 10.1038/nmeth.1290.
[38] K. Zhang, C.-K. Chou, X. Xia, M.-C. Hung, and L. Qin, “Block-Cell-Printing for live single-cell printing,” *Proceedings of the National Academy of Sciences*, vol. 111, no. 8, pp. 2948–2953, Feb. 2014, doi: 10.1073/pnas.1313661111.
[39] L. Ying, S. S. White, A. Bruckbauer, L. Meadows, Y. E. Korchev, and D. Klenerman, “Frequency and Voltage Dependence of the Dielectrophoretic Trapping of Short Lengths of DNA and dCTP in a Nanopipette,” *Biophysical Journal*, vol. 86, no. 2, pp. 1018–1027, Feb. 2004, doi: 10.1016/S0006-3495(04)74177-6.
[40] A. T. J. Kadaksham, P. Singh, and N. Aubry, “Dielectrophoresis of nanoparticles,” *Electrophoresis*, vol. 25, no. 21–22, pp. 3625–3632, Nov. 2004, doi: 10.1002/elps.200406092.
[41] I. Ermolina, H. Morgan, N. G. Green, J. J. Milner, and Yu. Feldman, “Dielectric spectroscopy of Tobacco Mosaic Virus,” *Biochimica et Biophysica Acta (BBA) - General Subjects*, vol. 1622, no. 1, pp. 57–63, Jun. 2003, doi: 10.1016/S0304-4165(03)00118-1.
[42] N. Manaresi *et al.*, “A cmos chip for individual cell manipulation and detection,” *IEEE J. Solid-State Circuits*, vol. 38, no. 12, pp. 2297–2305, Dec. 2003, doi: 10.1109/JSSC.2003.819171.

[43] X. Zhu, K.-W. Tung, and P.-Y. Chiou, “Heavily doped silicon electrode for dielectrophoresis in high conductivity media,” *Appl. Phys. Lett.*, vol. 111, no. 14, p. 143506, Oct. 2017, doi: 10.1063/1.4998751.
[44] J. Voldman, “Electrical forces for microscale cell manipulation,” *Annu Rev Biomed Eng*, vol. 8, pp. 425–454, 2006, doi: 10.1146/annurev.bioeng.8.061505.095739.
[45] M. Evander *et al.*, “Noninvasive Acoustic Cell Trapping in a Microfluidic Perfusion System for Online Bioassays,” *Anal. Chem.*, vol. 79, no. 7, pp. 2984–2991, Apr. 2007, doi: 10.1021/ac061576v.
[46] D. Bazou, W. T. Coakley, A. J. Hayes, and S. K. Jackson, “Long-term viability and proliferation of alginate-encapsulated 3-D HepG2 aggregates formed in an ultrasound trap,” *Toxicology in Vitro*, vol. 22, no. 5, pp. 1321–1331, Aug. 2008, doi: 10.1016/j.tiv.2008.03.014.
[47] I. Leibacher, P. Hahn, and J. Dual, “Acoustophoretic cell and particle trapping on microfluidic sharp edges,” *Microfluid Nanofluid*, vol. 19, no. 4, pp. 923–933, Oct. 2015, doi: 10.1007/s10404-015-1621-1.
[48] D. Ahmed *et al.*, “Rotational manipulation of single cells and organisms using acoustic waves,” *Nature Communications*, vol. 7, p. 11085, Mar. 2016, doi: 10.1038/ncomms11085.
[49] H. Bruus, “Acoustofluidics 7: The acoustic radiation force on small particles,” *Lab Chip*, vol. 12, no. 6, pp. 1014–1021, Feb. 2012, doi: 10.1039/C2LC21068A.
[50] L. Y. Yeo and J. R. Friend, “Ultrafast microfluidics using surface acoustic waves,” *Biomicrofluidics*, vol. 3, no. 1, p. 012002, Jan. 2009, doi: 10.1063/1.3056040.
[51] H. Bruus, “Acoustofluidics 2: Perturbation theory and ultrasound resonance modes,” *Lab Chip*, vol. 12, no. 1, pp. 20–28, Dec. 2011, doi: 10.1039/C1LC20770A.
[52] A. Marzo and B. W. Drinkwater, “Holographic acoustic tweezers,” *PNAS*, vol. 116, no. 1, pp. 84–89, Jan. 2019, doi: 10.1073/pnas.1813047115.
[53] K. Melde, A. G. Mark, T. Qiu, and P. Fischer, “Holograms for acoustics,” *Nature*, vol. 537, no. 7621, pp. 518–522, Sep. 2016, doi: 10.1038/nature19755.
[54] V. VanDelinder and A. Groisman, “Separation of Plasma from Whole Human Blood in a Continuous Cross-Flow in a Molded Microfluidic Device,” *Anal. Chem.*, vol. 78, no. 11, pp. 3765–3771, Jun. 2006, doi: 10.1021/ac060042r.
[55] F. Sabri, M. E. Sebelik, R. Meacham, J. D. Boughter, M. J. Challis, and N. Leventis, “In Vivo Ultrasonic Detection of Polyurea Crosslinked Silica Aerogel Implants,” *PLoS ONE*, vol. 8, no. 6, p. e66348, Jun. 2013, doi: 10.1371/journal.pone.0066348.
[56] I. Leibacher, S. Schatzer, and J. Dual, “Impedance matched channel walls in acoustofluidic systems,” *Lab on a Chip*, vol. 14, no. 3, pp. 463–470, 2014, doi: 10.1039/C3LC51109J.
[57] J.-H. Lee, K.-J. Lee, H.-G. Park, and J.-H. Kim, “Possibility of air-filled rubber membrane for reducing hull exciting pressure induced by propeller cavitation,” *Ocean Engineering*, vol. 103, pp. 160–170, Jul. 2015, doi: 10.1016/j.oceaneng.2015.04.073.
[58] R. A. Freitas, *Nanomedicine*. Austin, TX: Landes Bioscience, 1999.
[59] W. M. Haynes, *CRC Handbook of Chemistry and Physics, 92nd Edition*, 92 edition. Boca Raton, Fla.: CRC Press, 2011.

[60] P. B. Muller, R. Barnkob, M. J. H. Jensen, and H. Bruus, “A numerical study of microparticle acoustophoresis driven by acoustic radiation forces and streaming-induced drag forces,” *Lab on a Chip*, vol. 12, no. 22, p. 4617, 2012, doi: 10.1039/c2lc40612h.
[61] A. Kovalenko, M. Fauquignon, T. Brunet, and O. Mondain-Monval, “Tuning the sound speed in macroporous polymers with a hard or soft matrix,” *Soft Matter*, vol. 13, no. 25, pp. 4526–4532, 2017, doi: 10.1039/C7SM00744B.
[62] J. Friend and L. Yeo, “Fabrication of microfluidic devices using polydimethylsiloxane,” *Biomicrofluidics*, vol. 4, no. 2, Mar. 2010, doi: 10.1063/1.3259624.
[63] R. N. Palchesko, L. Zhang, Y. Sun, and A. W. Feinberg, “Development of Polydimethylsiloxane Substrates with Tunable Elastic Modulus to Study Cell Mechanobiology in Muscle and Nerve,” *PLOS ONE*, vol. 7, no. 12, p. e51499, Dec. 2012, doi: 10.1371/journal.pone.0051499.
[64] J. K. Tsou, J. Liu, A. I. Barakat, and M. F. Insana, “Role of Ultrasonic Shear Rate Estimation Errors in Assessing Inflammatory Response and Vascular Risk,” *Ultrasound in Medicine & Biology*, vol. 34, no. 6, pp. 963–972, Jun. 2008, doi: 10.1016/j.ultrasmedbio.2007.11.010.
[65] N. Nama, R. Barnkob, Z. Mao, C. J. Kähler, F. Costanzo, and T. Jun Huang, “Numerical study of acoustophoretic motion of particles in a PDMS microchannel driven by surface acoustic waves,” *Lab on a Chip*, vol. 15, no. 12, pp. 2700–2709, 2015, doi: 10.1039/C5LC00231A.
[66] W. S. Hanoosh and E. M. Abdelrazaq, *Polydimethyl Siloxane Toughened Epoxy Resins: Tensile Strength and Dynamic Mechanical Analysis*. .
[67] W. Xu, N. Chahine, and T. Sulchek, “Extreme Hardening of PDMS Thin Films Due to High Compressive Strain and Confined Thickness,” *Langmuir*, vol. 27, no. 13, pp. 8470–8477, Jul. 2011, doi: 10.1021/la201122e.
[68] M. Dorrestijn *et al.*, “Chladni Figures Revisited Based on Nanomechanics,” *Phys. Rev. Lett.*, vol. 98, no. 2, p. 026102, Jan. 2007, doi: 10.1103/PhysRevLett.98.026102.
[69] K. Latifi, H. Wijaya, and Q. Zhou, “Motion of Heavy Particles on a Submerged Chladni Plate,” *Phys. Rev. Lett.*, vol. 122, no. 18, p. 184301, May 2019, doi: 10.1103/PhysRevLett.122.184301.
[70] M. K. Tan, J. R. Friend, and L. Y. Yeo, “Direct visualization of surface acoustic waves along substrates using smoke particles,” *Appl. Phys. Lett.*, vol. 91, no. 22, p. 224101, Nov. 2007, doi: 10.1063/1.2814054.
[71] D. Hartono, Y. Liu, P. Lin Tan, X. Y. Sherlene Then, L.-Y. Lanry Yung, and K.-M. Lim, “On-chip measurements of cell compressibility via acoustic radiation,” *Lab on a Chip*, vol. 11, no. 23, pp. 4072–4080, 2011, doi: 10.1039/C1LC20687G.
[72] M. Evander *et al.*, “Noninvasive Acoustic Cell Trapping in a Microfluidic Perfusion System for Online Bioassays,” *Anal. Chem.*, vol. 79, no. 7, pp. 2984–2991, Apr. 2007, doi: 10.1021/ac061576v.
[73] D. Bazou, W. T. Coakley, A. J. Hayes, and S. K. Jackson, “Long-term viability and proliferation of alginate-encapsulated 3-D HepG2 aggregates formed in an ultrasound trap,” *Toxicology in Vitro*, vol. 22, no. 5, pp. 1321–1331, Aug. 2008, doi: 10.1016/j.tiv.2008.03.014.

[74] F.-M. Boisvert *et al.*, “A quantitative spatial proteomics analysis of proteome turnover in human cells,” *Molecular & Cellular Proteomics*, p. mcp.M111.011429, Jan. 2011, doi: 10.1074/mcp.M111.011429.
[75] E. Verneuil, A. Buguin, and P. Silberzan, “Permeation-induced flows: Consequences for silicone-based microfluidics,” *EPL*, vol. 68, no. 3, p. 412, Oct. 2004, doi: 10.1209/epl/i2004-10221-7.
[76] G. C. Randall and P. S. Doyle, “Permeation-driven flow in poly(dimethylsiloxane) microfluidic devices,” *PNAS*, vol. 102, no. 31, pp. 10813–10818, Aug. 2005, doi: 10.1073/pnas.0503287102.
[77] L. Gervais, N. de Rooij, and E. Delamarche, “Microfluidic Chips for Point-of-Care Immunodiagnostics,” *Advanced Materials*, vol. 23, no. 24, pp. H151–H176, 2011, doi: 10.1002/adma.201100464.
[78] D. Taller *et al.*, “On-chip surface acoustic wave lysis and ion-exchange nanomembrane detection of exosomal RNA for pancreatic cancer study and diagnosis,” *Lab on a Chip*, vol. 15, no. 7, pp. 1656–1666, 2015, doi: 10.1039/C5LC00036J.
[79] Y. Chen *et al.*, “Tunable Nanowire Patterning Using Standing Surface Acoustic Waves,” *ACS Nano*, vol. 7, no. 4, pp. 3306–3314, Apr. 2013, doi: 10.1021/nn4000034.
[80] Z. Tian *et al.*, “Wave number–spiral acoustic tweezers for dynamic and reconfigurable manipulation of particles and cells,” *Sci. Adv.*, vol. 5, no. 5, p. eaau6062, May 2019, doi: 10.1126/sciadv.aau6062.